Applicability of ultrasonic measurements to monitor and forecast stress change in subsurface storage applications

Chandra, Debanjan; Alghannam, Lujain; Barnhoorn, Auke

DOI
10.1016/j.enggeo.2025.108421

Publication date
2025

Document Version
Final published version

Published in
Engineering Geology

Engineering Geology 359 (2025) 108421

Contents lists available at ScienceDirect

Engineering Geology

journal homepage: www.elsevier.com/locate/enggeo

Applicability of ultrasonic measurements to monitor and forecast stress change in subsurface storage applications

Debanjan Chandra [a,b,*], Lujain Alghannam [a], Auke Barnhoorn [a]

[a] Department of Geoscience and Engineering, Delft University of Technology, Stevinweg 1, 2628 CN Delft, the Netherlands
[b] Department of Geosciences (IGV), Norwegian University of Science and Technology (NTNU), S. P. Andersens veg 15a, 7031, Trondheim, Norway

ARTICLE INFO

Keywords:
Cyclic loading
Triaxial failure
Ultrasonic velocity
Failure forecasting
Traffic-light scenario

ABSTRACT

The global expansion of subsurface CO_2 and hydrogen storage, alongside geothermal energy development, offers promising pathways for gigaton-scale CO_2 abatement. However, fluid injections and associated thermal effects can significantly alter reservoir stress states, risking fault reactivation and compromising caprock integrity. Direct stress measurements in the subsurface remain technically challenging, particularly beyond the near-wellbore zone. This study investigates how stress-induced changes in ultrasonic P- and S-wave velocities and amplitudes can serve as early indicators of irreversible rock deformation. Using triaxial cyclic and failure experiments on core samples from offshore Netherlands (depths: 3.1–4.2 km; porosity: 8–23 %), we demonstrate that wave velocities and amplitudes increase with axial loading in the elastic regime but decline progressively following crack initiation—well before mechanical failure. This trend reversal provides a reliable sonic precursor to failure. We propose a field-applicable traffic-light monitoring framework using sonic parameters to infer stress changes during injection operations. The observed inverse relationships between porosity and both mechanical strength and sonic velocity, along with the porosity-dependent velocity enhancement under confinement, present a novel opportunity to develop constitutive geomechanical models directly from reservoir sonic logs. This work advances non-invasive stress monitoring approaches and provides engineering geologists with robust tools to improve safety and predictability in subsurface energy storage projects. Moreover, such techniques can also be translated to integrity monitoring for underground mines and engineered structures.

1. Introduction

Carbon capture and storage (CCS) and shifting to low carbon energy alternatives like hydrogen and geothermal energy have been identified as the primary drivers to reduce atmospheric CO_2 level and arrest average global temperature rise within 2 °C of pre-industrial level (Lee et al., 2023). Subsurface porous reservoirs, which have historically been used for fossil fuel extraction, has gained new limelight for potentially sequestering huge volumes of H_2 (UHS) and CO_2 (Raji et al., 2023; Zhang et al., 2022a). With most European countries pledging to reach net-zero latest by 2050, the North-Sea has become a hotbed for emerging CCS projects (Gonzalez et al., 2021; Swennenhuis et al., 2020). Several western European countries along with USA have been identified as potential sites for H_2 storage with pilot projects in the pipeline (Sambo et al., 2022). Significant efforts on increasing geothermal resources in the energy mix is also happening globally (Lund and Toth, 2021). Mobile fluids like CO_2 and H_2 injections in depleted oil and gas reservoirs or saline aquifers cause stress perturbation, more precisely, by decreasing the effective overburden and horizontal stress. Such changes of reservoir pressure over a geologically short time can cause leakage along pre-existing faults into the seafloor or atmosphere. Additionally, percolation of injected fluids into the fault plane can alter the properties of fault plane, causing dilation, permeability enhancement, dissolution along fault plane and altering roughness along the fault-plane (Al Shafloot et al., 2024; Cornelio and Violay, 2020; Polak et al., 2004; Ramesh Kumar et al., 2023; White and Foxall, 2016; Zhang et al., 2023). Coupled effects of these changes lead to slip along the fault plane in reservoir or caprock, leading to seismicity, which has been observed in many geothermal, UHS and CCS projects worldwide (Buijze et al., 2019; Cheng et al., 2023; Majer et al., 2007; Rutqvist et al., 2016; Zang et al., 2014).

For any kind of reservoir operations, mechanical failure of reservoir or caprock is an extreme situation and should be avoided at all costs. Even before failure, irreversible or plastic deformation is accumulated within the reservoir when numerous microcracks form and merge within

* Corresponding author at: Department of Geoscience, Norwegian University of Science and Technology, S. P. Andersens veg 15A, 7031 Trondheim, Norway.
E-mail address: debanjan.chandra@ntnu.no (D. Chandra).

https://doi.org/10.1016/j.enggeo.2025.108421
Received 20 May 2025; Received in revised form 4 September 2025; Accepted 13 October 2025
Available online 14 October 2025

the storage and caprock formations. These microcracking events also cause seismicity and compromise the stability of the formation, which is detrimental in long-term fluid containment. Therefore, the operational pressure range for H_2/CO_2 storage projects are selected in such a way that the stress conditions can only cause elastic deformation of the reservoir. Pressure oscillation during periodic reservoir operations for UHS and geothermal projects might accumulate irreversible deformation in a reservoir over time. From a Mohr-Coulomb failure perspective, increase in pore pressure and a resultant decrease in effective stress reduces normal stress, while the shear stress remains constant. This shifts the Mohr circle towards the left and close to the elastic deformation zone and failure envelope (Choi et al., 2023; Park et al., 2022). The non-isothermal phase behavior of H_2 and CO_2 adds on to the complexity in reservoir stress path. Cold and liquid CO_2 is often injected at high pressure in hot reservoirs which expands due to pressure drop in depleted reservoirs and triggers Joule-Thomson cooling which causes cooling in the reservoir close to the injection well. Geomechanical and geochemical implications of extreme cooling in geological formations and also in wellbores have been studied in detail (Li and Pluymakers, 2024; Vilarrasa et al., 2014; Vilarrasa and Laloui, 2016; Vilarrasa and Rutqvist, 2017). Coupled effect of pore pressure increase and simultaneous cooling in the reservoir causes more vertical contraction compared to radial contraction (CLIMIT, 2020; Grande et al., 2024; Griffiths et al., 2021; Park et al., 2022), which brings the reservoir or caprock stress configuration close to failure. Therefore, studying the irreversible deformation behavior of reservoir and caprocks are of paramount importance for successful CCS projects. H_2 injection in the subsurface also triggers sudden temperature increase due to negative Joule-Thompson coefficient of H_2, however, its direct impact on stresses have not been explored in detail.

Deformation behavior of a rock mass can be easily studied in the laboratory using representative samples, where we can have good control on stress conditions. However, measuring stress change and plume movement over time is not so straight forward in the reservoir. There are several techniques to measure stress indirectly either from ground deformation using local strainmeter, tiltmeter or drone imaging and InSAR (Zhang et al., 2022b) or from in-situ deformation measurement using fiber-optics (Murdoch et al., 2020; Sun et al., 2021). More accurate and comprehensive geophysical tools like timelapse seismic surveys can provide exact movement of CO_2/H_2 plume, however such techniques are much more costly (Gasperikova et al., 2022). Timelapse sonic logging of P and S waves is a much more cost effective and simpler way to potentially monitor H_2/CO_2 plume migration, saturation of the reservoir and also its stress conditions (Le Ding and Song, 2016; Falcon-Suarez et al., 2016; Fortin et al., 2005; Janssen et al., 2021; Li et al., 2022; Müller et al., 2007; Sayers, 2002; Xue et al., 2009). Previous studies have shown at seismic frequency the presence of CO_2 in pore spaces instead of brine causes a large change in Vp (Agofack et al., 2018; Chen et al., 2013; Zhang et al., 2017), whereas ultrasonic velocity and amplitude measurements can help quantify even small deformation in rock mass. Apart from specific use cases in reservoir geomechanics, sonic attributes are widely used to quantify water saturation and effective stresses in soil and other rocktypes (Al-Shayea, 2001; He et al., 2021; Li et al., 2020). Deformation in subsurface formations and larger geoengineered structures are evaluated using 3D seismic and distributed acoustic sensing (DAS) techniques (Martínez-Martínez et al., 2016a; Nefeslioglu, 2013; Rossi et al., 2022; Williams et al., 2022; Xia et al., 2022). Theoretical approaches have proposed relationship between crack propagation and changes in sonic attributes based on petrophysical properties of host rock (Ersoy et al., 2019; Hamdi and Lafhaj, 2013; Li and Zhu, 2012; Martínez-Martínez et al., 2007, 2011).

Past CCS projects like Boundary Dam, Quest, Sleipner, In Salah and many others highlighted the importance of including stress monitoring in measurement, monitoring and verification (MMV) workflow. The high pore pressure development in Snohvit project (Hansen et al., 2013) prompted rapid development of remote stress monitoring using time-lapse seismic survey and decoupling the response of fluid migration and stress change (Grude et al., 2014). CO_2 leakage risk associated to the In Salah project indicated that integrated geomechanical modeling and understanding stress response of both reservoir and caprocks are of paramount importance in future CCS and UHS projects (Ringrose et al., 2013). On the other hand, stress monitoring also helps control leakage from wellbore and plume movement over time where multiple reservoir spaces are spatially connected. Complex geological areas like Gulf of Mexico is infested with active faults and around 1.1 million legacy wells pose risk of compromised wellbore integrity and pressure induced fault slip (Bump and Hovorka, 2024). In such cases, limiting stress evolution in the reservoir fairly under the reservoir fracture pressure(Bump and Hovorka, 2023; Zoback and Gorelick, 2015) is imperative. Microseismicities associated with other CCS projects globally also highlight that understanding the stress state before, during and after CO_2 injection needs to be understood in detail (Cao et al., 2021; Goertz-Allmann et al., 2014; Myer and Daley, 2011; Will et al., 2014). H_2 storage albeit at a nascent stage, also needs to account the learnings from CCS projects to ensure safe reservoir operation for a longer period.

In this study, we are focusing on the stress-dependent change in compressional and shear wave properties in sandstones of different porosity and depth collected from different locations of the Aramis CCS license area in the North Sea (Sorbier, 2024). Special focus will be given on how the P and S wave attributes respond to stress changes and elastic and plastic deformation. The primary objective will be to develop a benchmark between stress change and velocity change in porous sandstones to analyze their sensitivity with respect to porosity and develop a forecasting protocol to detect irreversible rock deformation during reservoir operations and propose a traffic light protocol based on change in wave attributes. The fundamental relationship between stress and sonic properties emerging from this study can be applied to any subsurface energy storage projects. The non-invasive monitoring technique proposed in this study can be applied to assess structural integrity of other subsurface or above-surface engineering geology projects.

Table 1
Details of samples collected along with their depth and porosity.

Well ID	Formation	Sample name	Replacement sample	Depth (m)	Porosity
K15–12	Upper Slochteren	K15–12-1V		3930.05	0.08
K15–12	Upper Slochteren	K15–12-12V		3945.1	0.14
K15–12	Upper Slochteren	K15–12-14V		3946.9	0.13
K15–12	Upper Slochteren	K15–12-21V		3955.8	0.09
K15–2	Lower Slochteren	K15–2-3V		3458.55	0.11
K15–2	Lower Slochteren	K15–2-4V		3458.72	0.11
K15–2	Lower Slochteren	K15–2-5V		3461.45	0.12
K15–2	Lower Slochteren	K15–2-7V	K15–2-2V	3462.35	0.12
K15-FG-102	Upper Slochteren	K15-FG-102-2V		4176.1	0.17
K15-FG-102	Upper Slochteren	K15-FG-102-4V	No suitable replacement found	4176.8	0.17
L09–10	Solling	L09–10-6VA		3172.2	0.22
K15-15A	Lower Slochteren	K15-15A-4V		4236.18	0.23
K15-15A	Upper Slochteren	K15-15A-6V		4236.81	0.19
K15-15A	Lower Slochteren	K15-15A-13V		4249.3	0.23

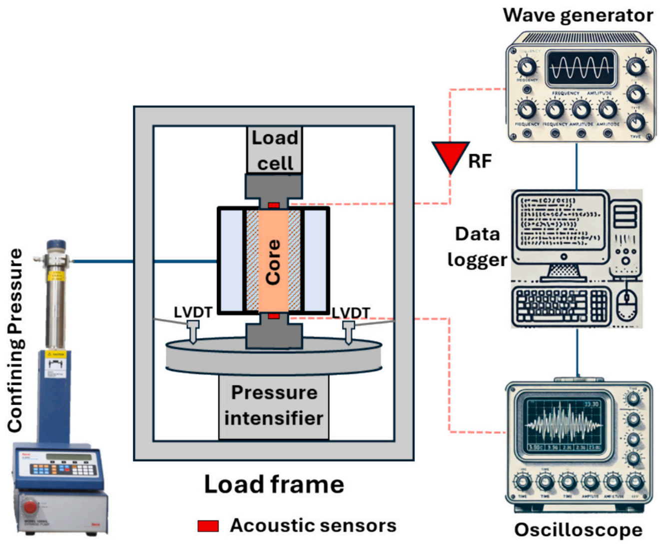

Fig. 1. Schematic of the experimental setup used for this study.

2. Methodology

2.1. Sample description

For the experiments mentioned in the following sections, the samples used were sandstone core plugs collected from different depths of Aramis license areas in the North Sea (specifically from the K15 and L9 blocks). More details of the sampling locations, coring wells and subsurface activities in those blocks can be found at https://www.nlog.nl/. The samples for the Aramis license area were provided by Shell through TNO (Nederlandse Organisatie voor Toegepast Natuurwetenschappelijk Onderzoek). Fourteen coreplugs having 1 in. diameter from different depths and different reservoir formations were collected for the experiments. The primary reservoir for K15 block is the Permian sandstones of Upper and Lower Slochteren Formations, which overlies the Base Permian unconformity (De Jager and Geluk, 2007). The thick evaporites of the Zechstein Group overlying the Upper Slochteren Formation works as a potential caprock for safe containment of CO_2. The Triassic Solling group is the primary reservoir for L9 block which unconformably overlies the Main Buntsandstein Subgroup, which is well cemented, providing good bottom-sealing. The Rot evaporite formation overlies the Solling sandstone, which acts an effective caprock (Geluk and Röhling, 1997). The samples and their descriptors are provided in Table 1.

Collected samples were first trimmed (if needed) and the end faces were polished to maintain a length-to-diameter ratio of 2 for the deformation experiments. Afterwards the core plugs (1″ diameter and 2″ length) were washed and dried in an oven for a day at 60 °C to remove the moisture accumulated during cutting and polishing. The porosity of the samples was measured with helium pycnometer before deformation experiments (Table 1). Reservoirs are usually saturated with brine and can have a salinity range of 0.1–20 wt%, however, most commonly the salinity is above 5 wt%. Since selecting a specific brine composition was not the focus of the study, we used a brine composed of 80 g/L NaCl (~8 wt%) to saturate the core plugs before deformation to simulate analogue reservoir conditions during the tests. The dried core plugs were put in a desiccator and vacuum saturated with brine for 12 h to remove air trapped in pore spaces and maximize brine saturation. It is worth mentioning that two of the chosen set of samples (Table 1) suffered damage while taking them out of the triaxial apparatus upon finishing the cyclic loading experiments (Section 2.2.1). For K15–2-7 V, we found

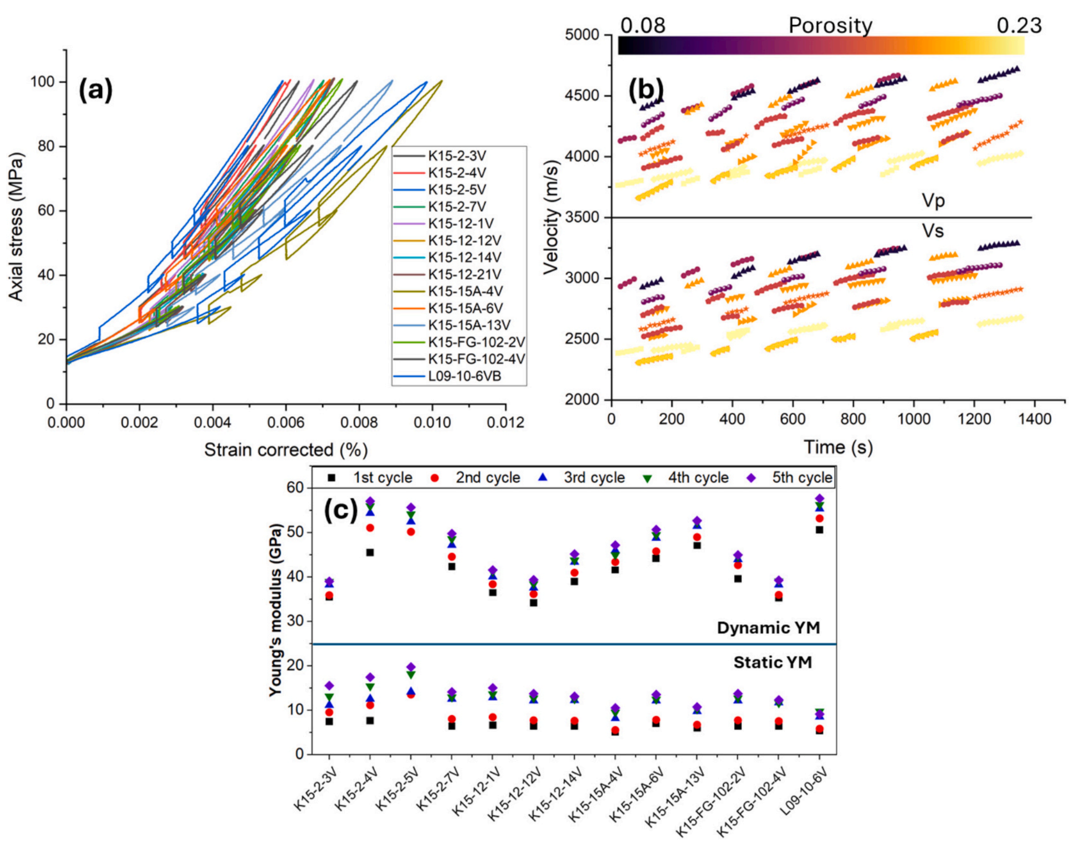

Fig. 2. (a) Stress-strain profile of cyclic axial loading and unloading experiments (b) Vp and Vs recorded in each cycle colored based on the porosity of corresponding coreplug (c) Static and dynamic Young's modulus for each specimen. (For interpretation of the references to colour in this figure legend, the reader is referred to the web version of this article.)

a replacement (K15–2-2 V) from a slightly shallower depth of the same well having same porosity, while no such suitable replacement was found for K15-FG-102-4V and was therefore not tested further for the failure experiments.

2.2. Experimental protocol

Deformation experiments conducted on the core plugs had two major goals: 1. Determine the change in P and S wave velocity during elastic deformation at different confining pressure and 2. Study the response of deformation behavior on the sonic attributes while the core plugs are undergoing elastic deformation to eventual failure at a fixed confining pressure. The first test protocol will give an idea of how the ultrasonic velocity of a rock mass will vary at different overburden stresses as the pore pressure increases due to pore fluid injection. The loading and unloading scenario also represent cyclic production and injection of H_2 in subsurface porous reservoirs at different depths. Whereas the second test protocol will help understand how the velocity response will change during inelastic deformation, essentially giving indications for the safe range of operating pressure for CCS and UHS projects. It is important to mention that during fluid injection, plastic deformation and subsequent failure of the reservoir rock are controlled by the reduction in effective stresses. Although in this study, we are using a different stress path than a realistic reservoir scenario, our main interest lies in investigating the sonic response during different stages of deformation and their controlling factors.

Similar to any geological formation, even within the same reservoir, sandstones vary in mineral composition, porosity, depositional conditions any many other parameters. Since the deformation and wave propagation behavior vary significantly due to these factors, our goal was to use the same coreplug for both test routines mentioned above. Since the first test routine will induce negligible permanent deformation in the sample, we assume that the sample is nearly pristine for the second set of experiments.

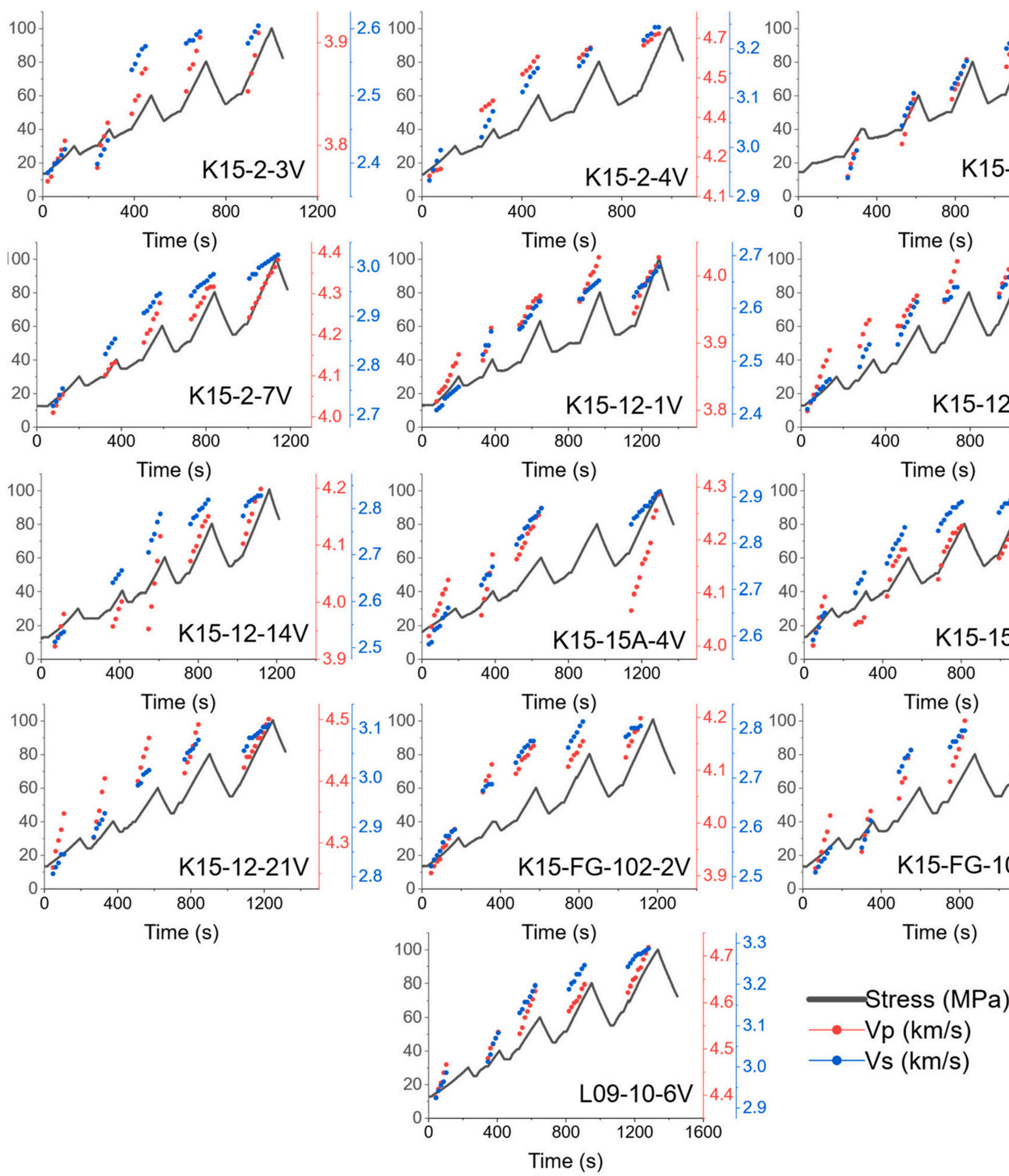

Fig. 3. Axial Vp and Vs plotted in a time-series during cyclic axial loading-unloading experiments. (For interpretation of the references to colour in this figure legend, the reader is referred to the web version of this article.)

All triaxial deformation experiments were carried out at room temperature using a customised Hoek-cell coupled with a 500 kN axial loading frame developed at TU Delft (Fig. 1). A detailed description of this setup can also be found in (Naderloo et al., 2023; Veltmeijer et al., 2024). Vacuum-saturated coreplugs were placed within the Viton sleeve inside the Hoek-cell, and an ISCO model 100DM syringe pump was used for regulating confining pressure. A top and bottom piston was added for applying axial deformation on the coreplugs (Fig. 1). The pistons were made of stainless steel to minimize piston deformation during the experiments. Fluids channels were made along the periphery of the piston to allow fluids to escape during compaction, allowing drained condition. One S wave piezoelectric transducer with a diameter of 10 mm, and a thickness of 5 mm having a central frequency of 1 MHz was housed inside each piston, to measure timelapse ultrasonic properties of the coreplugs along the axial direction. A small component of the shear wave energy from the source transducer converts to compressional wave at the contact between anisotropic media (in this case between transducer-piston-specimen), resulting in small vertical displacement. This converted mode is recorded at the receiver and attributed as the P wave arrival time for the experiments. One of the transducers acted as a source and was connected to an Agilent 33210A waveform generator, generating sine waves of 800 mV peak-to-peak and 50 Ω impedance, which was further amplified by a 1 kV RF power amplifier. The receiver was connected to a Yokogawa DL9240L oscilloscope and a datalogger recording time-lapse waveforms every 15 s for 100 μs and averaged over 512 stacks to enhance the signal-to-noise ratio. The recorded waveforms were further processed with RadexPro seismic processing software to determine P and S wave arrival times and corresponding amplitudes after correcting for the travel time within the pistons. Axial loading in the setup is applied by moving the bottom platen of the load cell, while the top remains fixed. Two linear variable displacement transformers (LVDT) with a maximum limit of 2 mm were connected to the bottom platen of the load cell to measure and regulate the displacement, and a constant deformation rate of 0.0005 mm/s was applied to build axial stress on the coreplugs. Due to the design of the experimental setup, it was not possible to measure radial deformation.

Before the experiments, the instrument deformation was calibrated using a steel plug of known Young's modulus. Instrument deformation was deducted from the total deformation for each experiment mentioned in the following subsections. Details about the two different protocols are explained separately in the following subsections:

2.2.1. Cyclic axial loading with incremental confinement

The first set of experiments were to induce elastic deformation on the coreplugs at different confinements and measure the change in sonic properties during deformation. Five stages of cyclic axial loading experiment were planned with confining pressure ranging from 10 to 50 MPa with an increment of 10 MPa between each stage. Vacuum-saturated core plugs were loaded into the Hoek cell and slowly brought to a 10 MPa hydrostatic condition. In each confining pressure we decided to increase the axial stress up to 2× confining pressure to minimize any permanent change in the coreplug but also have enough mechanical and sonic dataset to draw meaningful inferences. The only exception was the first cycle, where the peak axial stress was 3× confinement to ensure we elastically load the coreplug beyond primary consolidation. It is worthwhile to mention that the sonic data were recorded for the loading stages only. Once the peak load (2× confinement) in a corresponding cycle is achieved, the axial load was slowly reduced to match the hydrostatic condition for the next cycle. The confining pressure was then increased until a hydrostatic stress condition was achieved, and the axial loading was repeated following the previous step. For example, at 20 MPa confinement, we bring the axial stress to 40 MPa, then unload it to 30 MPa. The confinement then increases to 30 MPa and we ramp the axial stress to 60 MPa. This protocol was repeated for five cycles.

2.2.2. Axial loading till failure at fixed confinement

For the second set of experiments, the samples used for Section 2.2.1 were reused so that the material properties for both experiments are the same, assuming negligible plastic deformation took place during the cyclic loading tests as evidenced from the ultrasonic velocities (section 3.1.2). The samples were re-saturated before they were loaded into the Hoek cell, and a hydrostatic stress condition of 40 MPa was imposed on the coreplugs. A generic effective horizontal stress gradient of 10 MPa/km was assumed for estimating in-situ stress condition of the samples. As evident from Table 1, all samples belong to a depth range of 3–4 km, hence an effective confining stress of 40 MPa was assumed for all samples to maintain uniformity in experimental protocol. The core plugs were axially loaded starting from a hydrostatic condition and brought to failure. The objective of these experiments was to study the change in sonic properties during elastic and plastic deformation.

3. Results

3.1. Cyclic loading experiments

3.1.1. Stress-strain behavior

The stress-strain behavior of the cyclic loading experiments can be found in Fig. 2a. Loading and unloading in each confinement is indicated by each hysteresis loop. It is interesting to see that all samples have different loading profile, depending on their porosity. An inverse relationship between porosity and Vp, Vs of the plugs is also observed at each confinement (Fig. 2b). Plugs with lower porosity have steeper loading profile and accumulate less strain and vice versa, especially at higher confining pressure. The hysteresis between the loading-unloading profile indicates that there is some irreversible deformation within the plugs, even within elastic deformation regime, more significant in higher confinement and for high-porosity samples. This behavior is also observed by other researchers (Naderloo et al., 2023; Pijnenburg et al., 2018, 2019; Shalev et al., 2014), where hysteresis could be seen

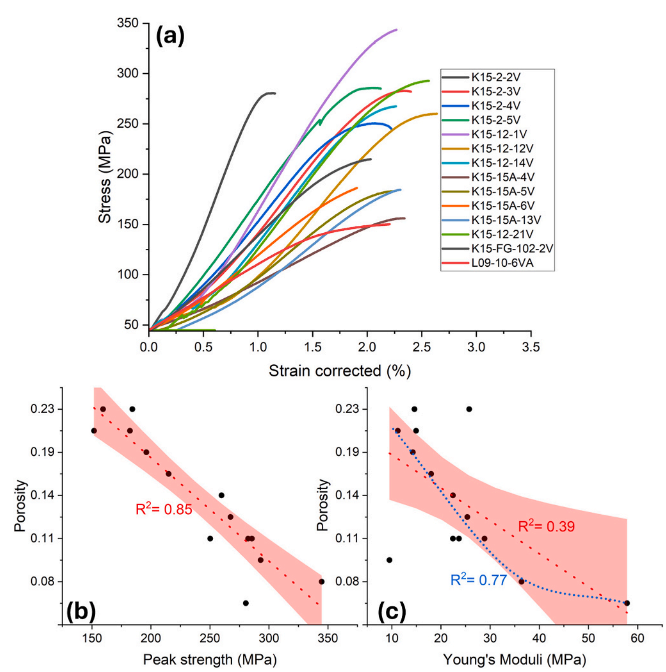

Fig. 4. (a) Deformation behavior of the coreplugs during failure experiments under constant confinement, (b) Correlation between porosity and peak strength of the coreplugs and (c) linear (red dotted line) and non-linear (blue dotted line) correlation between porosity and Young's moduli. The red shaded regions indicate 95 % confidence interval of the linear fit. (For interpretation of the references to colour in this figure legend, the reader is referred to the web version of this article.)

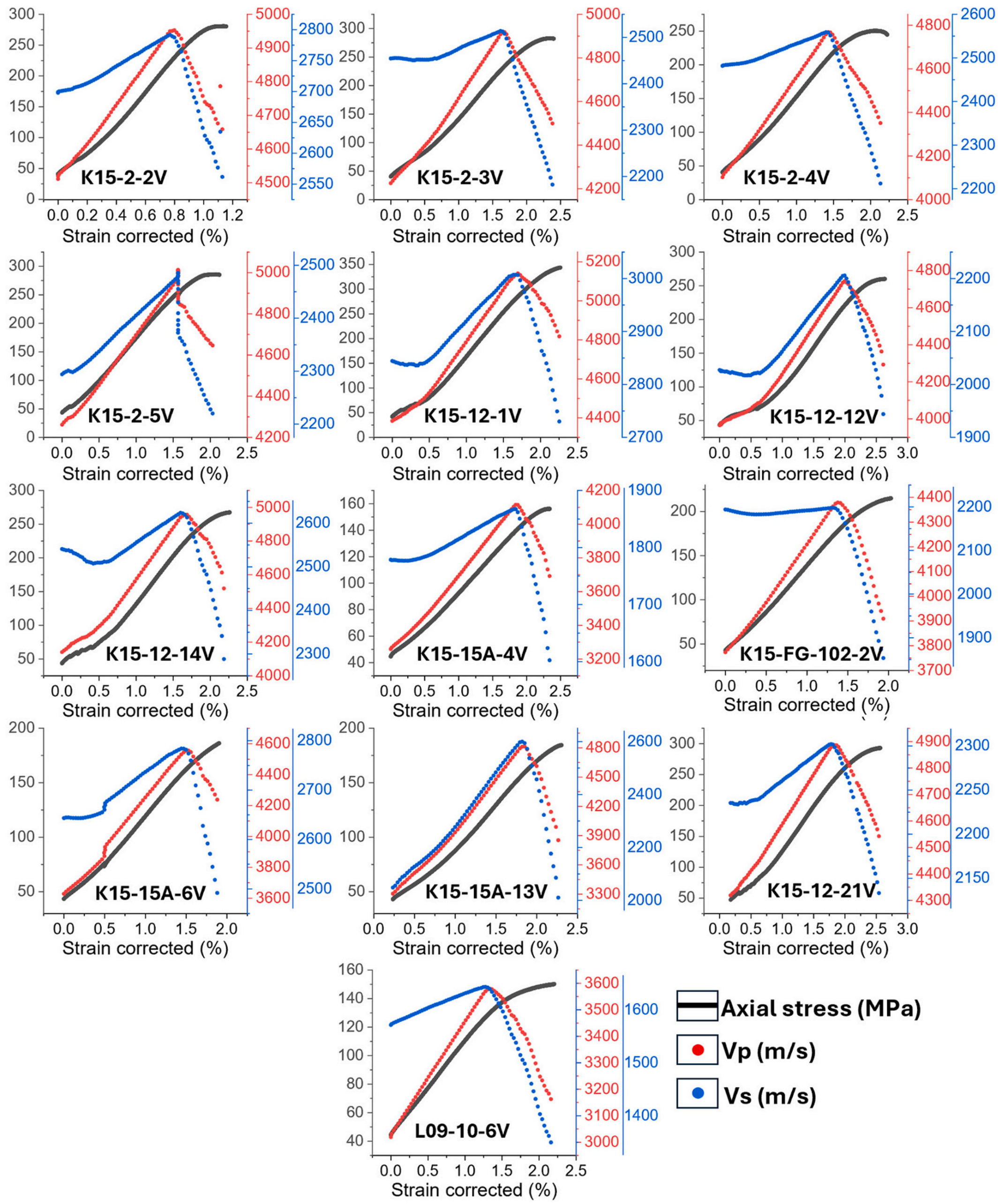

Fig. 5. Change in axial Vp and Vs with progressive deformation during triaxial failure experiment. Y axis on the left indicates axial stress, whereas the two axis on the right indicate Vp and Vs (coded by blue and red). (For interpretation of the references to colour in this figure legend, the reader is referred to the web version of this article.)

while stress cycling below the yield stress or low deviatoric stress, and maximum accumulation of inelastic strain is during the first cycle. The extent of hysteresis is strongly dependent on the porosity and pore fluid composition and is caused by the compaction recovered by inelastic dilation in the unloading stage, however this does not indicate any grain-scale deformation (Shalev et al., 2014; Tutuncu et al., 1998). The static Young's modulus (E_{stat}) and dynamic Young's modulus (E_{dyn}) were calculated for each cycle (Fig. 2c) using the following equations (eq. 1a, b)

$$E_{stat} = \frac{\Delta\sigma_1}{\Delta\varepsilon_1} \tag{1a}$$

$$E_{dyn} = \frac{\rho V_s^2\left(3V_p^2 - 4V_s^2\right)}{V_p^2 - V_s^2} \tag{1b}$$

Where $\Delta\sigma_1$ and $\Delta\varepsilon_1$ are change in axial stress and axial strain in a linear interval considering a fixed confinement. ρ is the matrix density of the coreplugs which is calculated from helium porosimetry. As indicated by earlier studies (Brotons et al., 2016; Fjær, 2009; King, 1969; Wang et al., 2020), E_{dyn} is generally higher than E_{stat}, especially at higher frequencies, as smaller pores and fractures appear stiffer at higher frequencies. As expected, both static and dynamic YMs increase with increasing confinement.

During the experiment, to limit the deformation of the sample, the position of the axial pistons was kept fixed between the end of unloading stage and the beginning of the next loading stage. The increase in confinement during this brief period caused a small increase in stress. Due to technical difficulties, the first cycle of loading (at 10 MPa confinement) could not be performed for K15–2-5V.

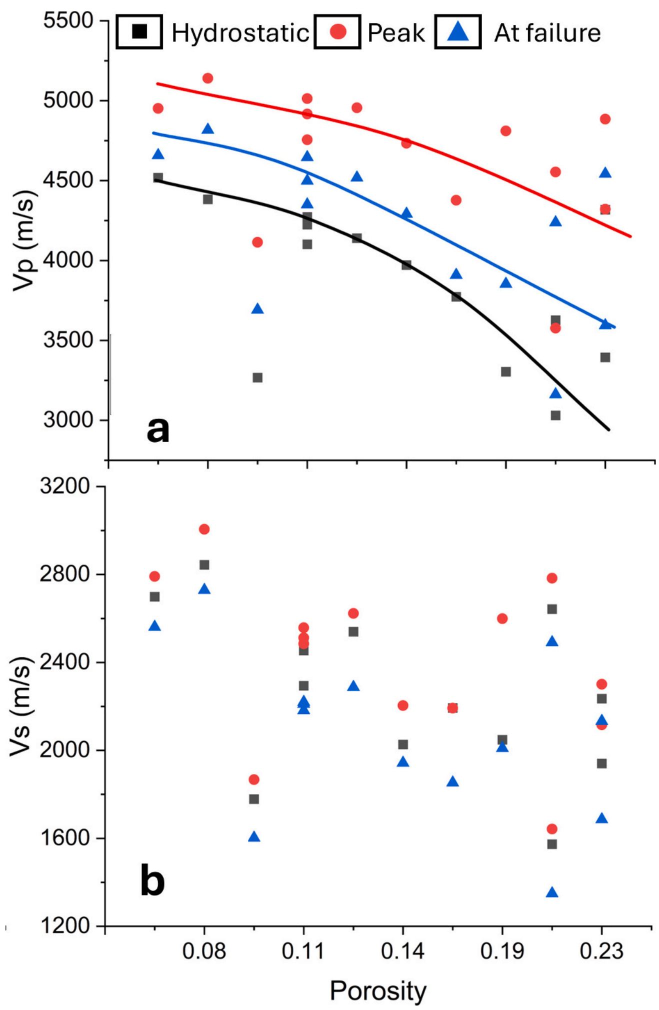

Fig. 6. Change in (a) Vp and (b) Vs for plugs of different porosity during failure experiment. (For interpretation of the references to colour in this figure legend, the reader is referred to the web version of this article.)

3.1.2. Change in sonic properties

As mentioned before, ultrasonic waves transmitted through the coreplugs were recorded throughout the loading stages of the experiments with an interval of 15 s (Fig. 2b). The change in sonic properties in different cycles can be seen in Fig. 3. A general observation for all samples is that both P and S wave velocity increases with increasing hydrostatic stress, which is also expected as majority of pre-existing microcracks and pores get compressed with increasing hydrostatic stress (Guo et al., 2009; Mavko et al., 2012; Wei and Fu, 2014). This leads to an increase in density of the rock mass, which in turn increases the compressional and shear wave velocity. However, it is interesting to note that the rate of increase in velocity slows down with progressive hydrostatic stress beyond 30 MPa as the rockmass approaches the limit of its compression as most pre-existing fractures are closed. Such behavior is observed in other rock types, where increasing hydrostatic compaction increases the velocity quickly in the beginning and slows down as the rock approaches maximum elastic compaction. Beyond critical compaction, increasing hydrostatic stress can cause pore collapse (for porous rocks) and yielding, which causes grain contacts to fail plastically. Previous studies on other types of sedimentary and crystalline rocks (Fortin et al., 2011; Nasseri et al., 2009; Yang et al., 2021) have shown a nonlinear increase in wave velocity with increasing hydrostatic stress. It is worthwhile to mention that there is no acoustic data for the fourth cycle deformation of K15-15A-4V.

3.2. Triaxial failure experiments

3.2.1. Stress-strain behavior

The cyclic loading experiments discussed above provide a baseline for elastic deformation behavior. The subsequent failure tests build upon these results to capture inelastic deformation and velocity attenuation. Samples which underwent cyclic loading-unloading were further brought to failure at a fixed confining pressure (40 MPa). For all failure experiments, the loading curve till the peak stress is shown in Fig. 4. The peak stress of the coreplugs varies widely between 153 and 342 MPa. The loading rates were the same as the cyclic loading tests. The deformation behavior of the coreplugs vary significantly due to their inherent differences in petrophysical properties and the Young's moduli (YM) varies between 11 and 58 GPa. A very good correlation was observed between the porosity and peak strength of the plugs, whereas a relatively weaker linear correlation was found between porosity and YM of the plugs which was also confirmed by similar studies (Hamada and Joseph, 2020; Hart and Wang, 1995; Palchik, 1999).

3.2.2. Change in sonic properties

The velocities and axial stress show concurrent linear increase till the yield stress. After yield stress, the rate of stress increase is slower and the compressional and shear wave velocity shows rapid decline (faster than the rate of increase) (Fig. 5). At the point of failure, Vs is in most cases much lesser than the hydrostatic Vs due to more crack generation along the loading direction, which significantly attenuates S wave propagation (Barnhoorn et al., 2018; Zhubayev et al., 2016). Vp also decreases significantly but doesn't fall below hydrostatic Vp. It was expected that both P and S wave velocity will increase unimodally during the elastic compression stage, however, a minor drop and further rise in Vs was observed in the initial loading stage. Most often, the specimen goes through a pre-compaction initial settling within the load cell as evident by the slow load buildup preceding the linear stress-strain profile, which contributes to the minor fluctuation in the arrival times. For some experiments, the increase in Vs is minimal between hydrostatic loading and peak Vs, which corroborates with the findings of (Zaima and Katayama, 2018).

3.3. Change in ultrasonic velocity as a function of stress-state

Attenuation of the compressional and shear waves due to changes in stress conditions causes a drop in velocity and amplitude which can indicate the deformation behavior of the rockmass. Increase in wave velocities signifies an increase in density, therefore closure of pre-existing cracks and pores in the rockmass. The rate of increase in velocity also depends on the orientation of the pre-existing crack or anisotropy of the pore geometry (Ashby and Hallam, 1986; Griffiths et al., 2017). The coreplugs used for this study had different porosity, however, they also had different grain sizes, mineralogy and varied degree of anisotropy despite all being sandstones, which also affect the deformation behavior of these plugs (Qi et al., 2022; Rice-Birchall et al., 2022; Shahsavari and Shakiba, 2022; Sujatono and Wijaya, 2022). The failure experiments suggest that there is a good correlation between the porosity and hydrostatic Vp of the coreplugs, however, the correlation becomes weaker between porosity and max Vp (Fig. 6a). Nevertheless, comparing both the fitting curves indicate that the difference in max Vp and hydrostatic Vp is much more pronounced for higher porosity sandstones. A conclusive correlation could not be found for Vs (Fig. 6b), which may have been caused due to varied degrees of pre-existing cracks in these samples.

The temporal change in velocity and stress both are usually highest in the initial phase of axial loading in each cycle starting from hydrostatic condition. This is expected, since the stiffness of the coreplug is least at lower deviatoric stress and gradually increases with increase in deviatoric stress within the elastic deformation regime. This behavior is also reflected in the velocity response with stress (Fig. 7) where incremental change in stress and velocity is quantified in each cycle of loading. For low porosity samples, the rate of change in velocity is often similar in all cycles, indicating that the stiffness of the samples at hydrostatic condition at each confining stress is similar (Fig. 7a). Theoretically low porosity samples have lesser pore spaces to squeeze and hence they reach optimum stiffness at even lower confinement. For higher porosity sandstones, porosity decreases exponentially with increasing in hydrostatic confinement (Fig. 7c) which is also explained by Xu et al. (2018). Porosity is inversely proportional to the rate of change in wave velocity, i.e. at higher stiffness the rate of change in wave velocity will be lesser, which is evident from our experiments. For higher porosity sample, we see a gradual decrease in rate of change in Vp with each consecutive cycle, which indicates that all pores are yet to be squeezed even at 50 MPa hydrostatic confinement. Also, it is worth noting that for K15-15A-13V, the rate of change of Vp in lower confinement is higher than other low porosity counterparts.

The rate of change in velocity is evidently much more significant when the samples are axially loaded beyond elastic stress regime (Fig. 8). It shows that the rate of increase in axial stress decreases uniformly till the point of failure (except the initial settling phase) under constant axial deformation rate. However, the rate of change in velocity remains constant in the elastic deformation regime and suddenly drops at the elastic-plastic transition zone just before the trend reversal. After the trend reversal the rate of change keeps increasing till the point of failure (shown in negative, since the velocity monotonically decreases after the trend reversal).

3.4. *Waveform amplitude as a function of stress-state*

Change in elastic wave velocity can be caused by multiple reasons. Change in pore fluid composition during fluid injection can cause a reduction in velocity as the H_2 or CO_2 front (liquid or gas) displaces the reservoir brine which is significantly denser (Delle Piane and Sarout, 2016; Falcon-Suarez et al., 2020; Ghosh and Sen, 2012; Nooraiepour et al., 2018). Therefore, in an operational reservoir, it is difficult to pinpoint if reduction of Vp and Vs is caused by formation of cracks within the reservoir or due to displacement of reservoir brine by lighter fluids. To calculate the peak amplitude at the P and S wave arrival (termed hereby Pamp and Samp respectively), we selected a 10 μs symmetric window around P and S wave arrival picks respectively and the maximum amplitude (either positive or negative polarity) is selected as the peak amplitude of that trace. Since S wave transducers were used for these experiments, the P wave amplitude (Pamp) is much weaker compared to the S waves (Samp) (Fig. 9). Interestingly, even though the Vp and Vs trend reversal occurs concurrently during the experiments, peak Pamp and Samp occur at different times. In most cases, peak Pamp can be seen at the same time as max Vp and Vs (indicated by the green bars), however, peak Samp occurs much before that point.

Apart from the time difference between velocity and amplitude response, especially for S waves, there are some key differences on how Samp changes throughout the deformation. In Fig. 5, we can see in some cases the change in Vs is insignificant between hydrostatic Vs and peak Vs, but there is significant drop in Vs from peak Vs to Vs at peak axial stress, which is often much lower than hydrostatic Vs. However, in Fig. 9, we can see that both the increase and drop in Samp is noticeable for all samples irrespective of their porosity but the Samp at peak axial stress never goes below hydrostatic Samp. This indicates that the attenuation of S waves due to formation of cracks impacts the travel time more than the amplitudes. The magnitude of increase in Pamp and Samp from hydrostatic condition to peak values show good correlation with the porosity of the coreplugs (Fig. 10).

The relative change in velocity and amplitude during deformation shows different behavior based on their porosity (Fig. 11). In all cases, the amplitude changes relatively slowly in the beginning despite the increase in velocity, however as the plugs achieve their peak velocity, the amplitude increases rapidly. As the velocity decreases and more cracks appear in the plugs, the amplitude also decreases, forming a hysteresis loop, but never goes below the initial amplitude. For low and medium porosity samples (Fig. 11 a,b) the change in Vp is more dominant than Pamp, whereas the change in Samp is more dominant than

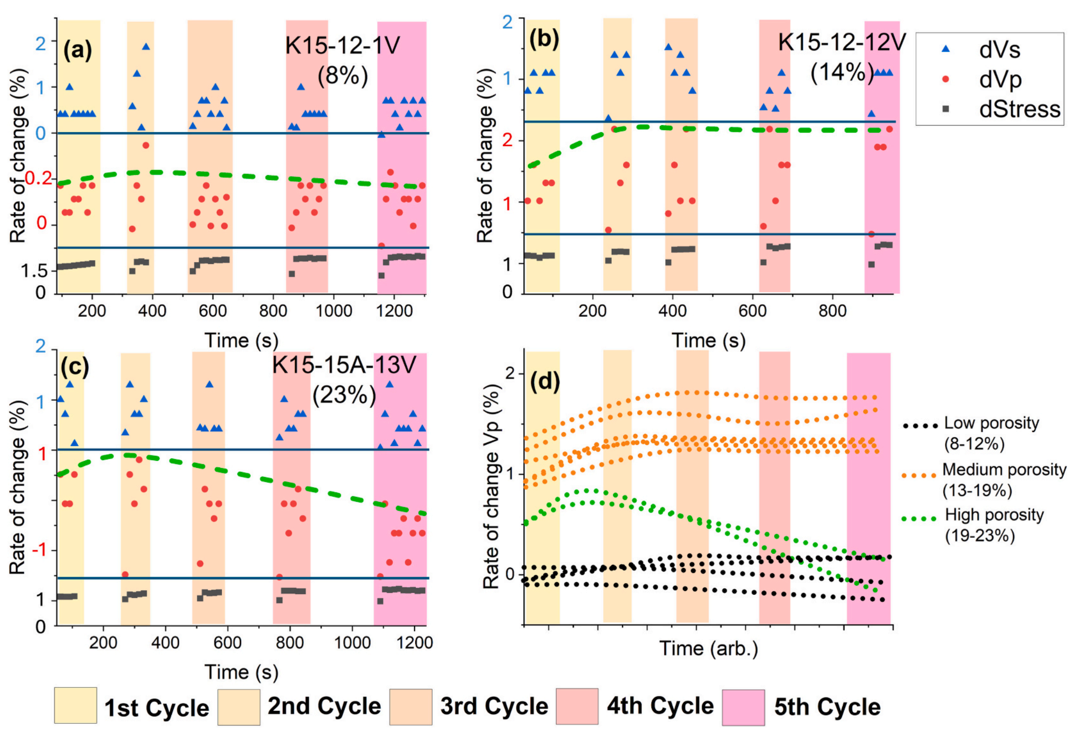

Fig. 7. Rate of change of axial stress (dStress), Vp (dVp) and Vs (dVs) for three representative plugs, each belonging to (a) low, (b) medium and (c) high porosity groups. (d) shows the rate of change of Vp for all studied coreplugs grouped by porosity. The green dotted lines in a, b and c indicate the best-fit of dVp across all cycles. (For interpretation of the references to colour in this figure legend, the reader is referred to the web version of this article.)

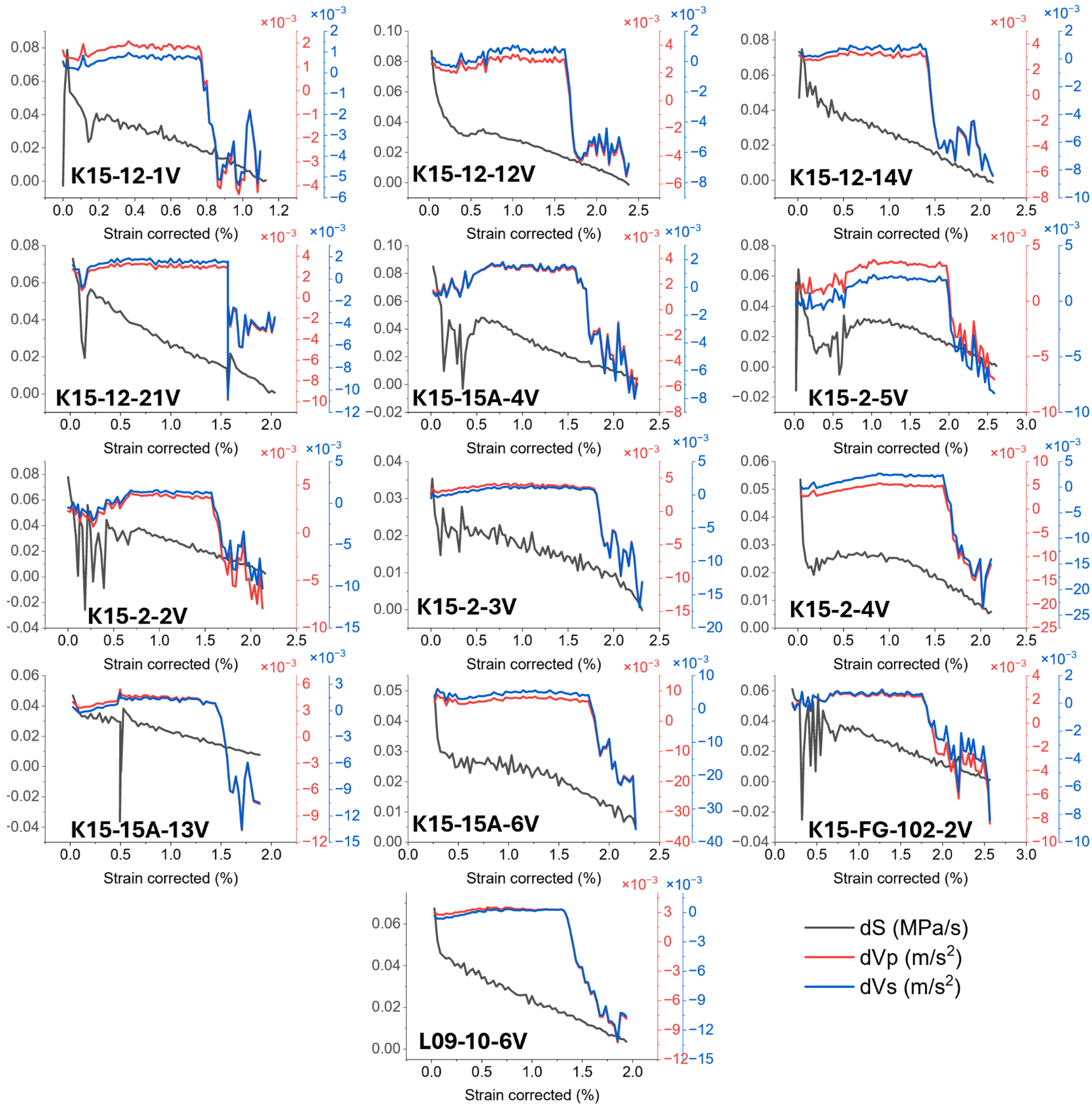

Fig. 8. Rate of change of stress and corresponding rate of change in Vp and Vs during the failure experiments. dS indicate incremental change in axial stress, whereas dVp and dVs indicates incremental change in P and S wave velocity respectively. (For interpretation of the references to colour in this figure legend, the reader is referred to the web version of this article.)

change in Vs. The relative change in Samp is also of higher magnitude in low and medium porosity samples, and is more evident when grouped together based on their porosity (Fig. 11 d,e).

4. Discussion

4.1. Applicability for reservoir scale geomechanical model

The experiments performed in this study combined the synchronous development of mechanical and sonic properties in a porous rockmass. The specimens collected had diverse anisotropy, grain size and porosity, which is expected in a reservoir across different depths. Among these different petrophysical properties, porosity emerged as one of the parameters which justify the diverse mechanical and sonic behavior of the sandstones. Sonic and mechanical behavior during cyclic loading explained in section 3.1 highlights that the change in Vp and Vs with increasing confinement is very different for low, medium or high porosity samples (Fig. 7). Low-frequency P and S wave attributes measured in the subsurface can monitor changes in fluid saturation (Caspari et al., 2011; Nakajima et al., 2019; White et al., 2017; Xue et al., 2006), however the changes in wave attributes not only reflect changes in fluid composition or saturation, but also contains signature of stress change in the reservoir (Mayr and Burkhardt, 2006). Testing different reservoir samples at their in-situ horizontal stress condition along with cyclic loading at different confinements can give us the upper and lower bound of safe velocity zones once the effective confining pressure drops during injection (Fig. 12).

This can be matched with a depth vs pressure log collected from the subsurface and a combined interpretation can be used for constructing a geomechanical model of the reservoir. Velocity dependence on grain size, cementation, pore size and in-situ fluid composition can be derived, and using such correlations, a sonic-mechanical model can be

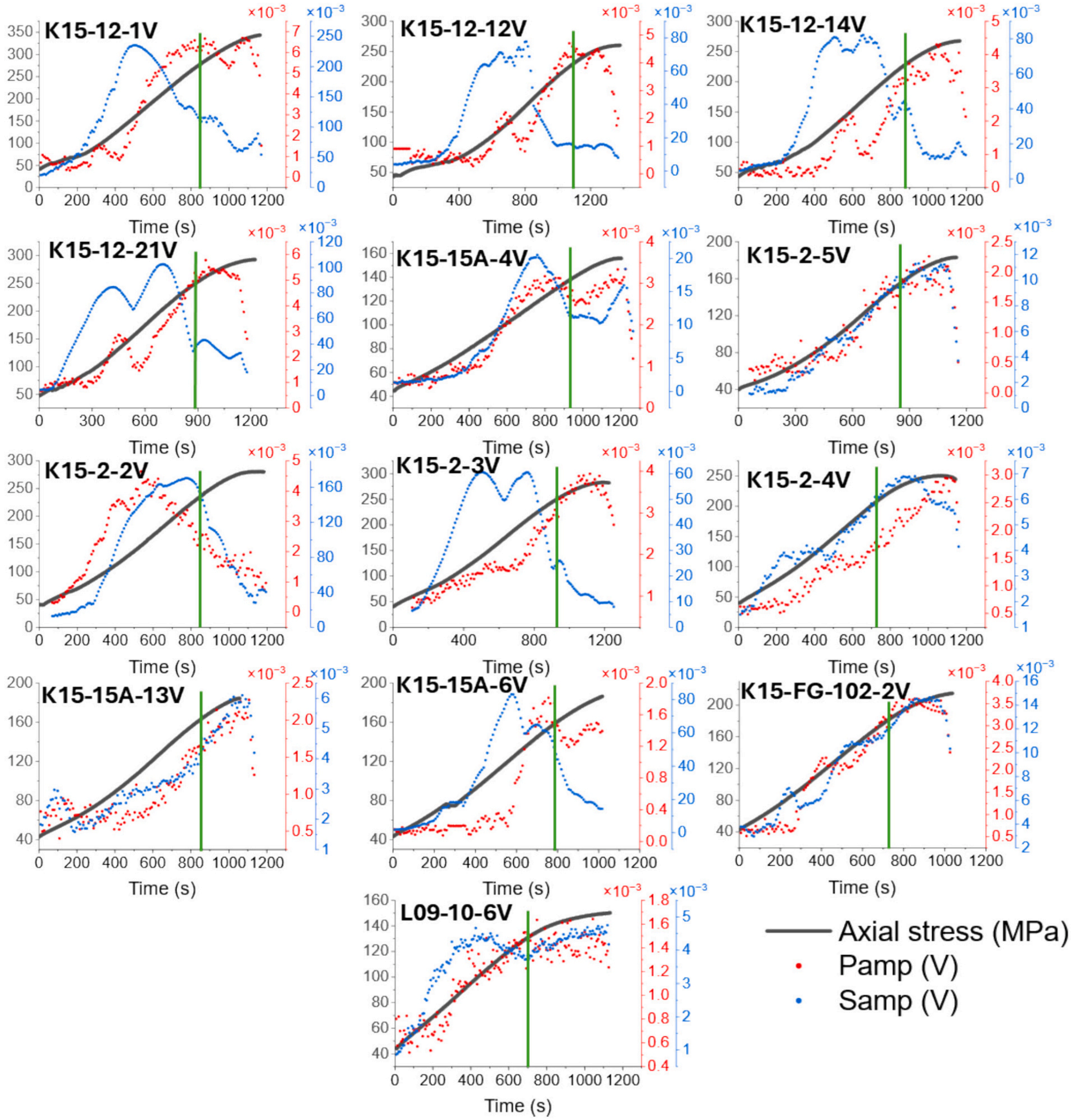

Fig. 9. Change in peak amplitude at P wave (Pamp) and S wave (Samp) arrival during the failure experiments. The green vertical bars in each plot indicate the time of max Vp and Vs for these experiments. (For interpretation of the references to colour in this figure legend, the reader is referred to the web version of this article.)

formulated for other reservoirs. A major challenge for such seismic monitoring is that actual S-wave velocity data are limited, particularly in 4D seismic data for CO_2 sequestration and possibly for H_2 injection, because wells are closed after injection (permanently for CO_2 storage and periodically for H_2 storage), and while seismic monitoring continues, no well log data are collected (Li et al., 2017). S wave velocity is often obtained through empirical models based on Vp, however, our studies indicate that although Vp and Vs show similar behavior with stress change, the amplitudes behave very differently throughout the test. Therefore, having S wave measurements in the subsurface during and after fluid injection can give us useful information about the stress path of the reservoir. Same can be applied for caprocks as well.

4.2. Deformation monitoring and forecasting

Laboratory experiments of representative reservoir rocks can help us understand the permissible change in velocity within elastic deformation zone and help delineate the critical velocity zone. However, velocity alone might not be the best indicator for reservoir deformation during H_2 or CO_2 injection, since displacement of brine with lighter fluids significantly decreases the Vp and Vs due to their lower density and such behavior is often leveraged to monitor saturation of fluids in the reservoir. Although velocity change with saturation can be explained with Gassman model (Gassman, 1951) and its modified approaches (El-Husseiny et al., 2019; Falcon-Suarez et al., 2018; Li et al., 2017; Nooraiepour et al., 2017), and any deviation in the velocity change can be attributed to a coupled effect of flow and deformation as demonstrated by Chandra and Barnhoorn (2025). The bounds in velocity change due to change in fluid density or deformation can be benchmarked through lab experiments and can be further applied to the field. Amplitude on the other hand also decreases both due to displacement of brine or plastic deformation, and therefore needs to be studied in detail through

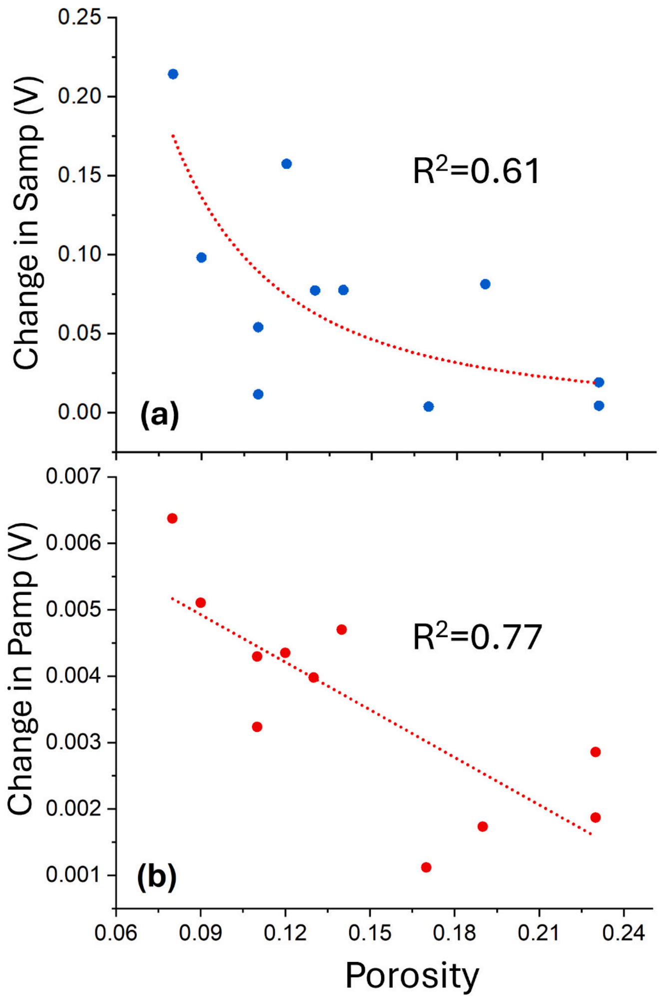

Fig. 10. Difference between maximum and minimum (a) Samp and (b) Pamp during the failure experiments and their correlation with porosity of the coreplugs.

laboratory experiments. As discussed before, rapid cooling near wellbore during CO_2 injection also prompts sudden increase in shear stress, leading to crack formation and in those cases, change in mechanical properties of the rock plays dominating role on velocity and amplitude compared to change in fluid composition. Based on combined velocity and amplitude, we can delineate how safe/unsafe a certain magnitude of differential stress is (Fig. 13). Here we explain how a traffic light system can be developed with K15–12-1V as an example.

Based on P wave velocity, we can easily indicate that a drop in velocity followed by a period of increase indicates approaching proximity to failuree (Zone 4), since further increase in differential stress will create more fractures, eventually leading to failure (Fig. 13a). With the rate of axial deformation chosen for this study, the time difference between peak Vp, Vs and failure is 297 s. The zone where both amplitude and velocity are increasing with a constant rate, can be termed as the safe/green zone (Zone 1). Samp peaks much before Vs, so a trend reversal in Samp can be an indicator that the green zone has passed, and we are approaching irreversible deformation. Based on this analogy, Samp trend reversal can be termed as the start of yellow zone (Zone 2). In most cases Vp and Pamp peaks at the same time, so Zone 2 is not visible when using only P wave attributes for interpretation. Zone 2 continues till the point where the rate of Vp and Vs change drops rapidly. This can be used as a precursor to impending velocity reversal, so the time between the trend reversal in dVp/dVs and Zone 4 can be indicated as orange zone (Zone 3). It is worthwhile to mention that Zone 2 and Zone 3 starts 370 s and 63 s respectively before onset of Zone 4. In reservoirs, the rate of change in stress is an order of magnitude slower compared to laboratory experiments and thus the precursors might be observed days or months before the onset of microcracks in the reservoir. However, the applicability of this technique is not limited to reservoir engineering projects and can be easily applied to monitor structural health of tunnels, bridges or changes in stress distribution in underground mines. Instances of using elastic waves for other engineering projects have been demonstrated in several literatures (Che et al., 2015; Deng et al., 2023; Falls and Young, 1998; Gladwin, 1982; Lu and Michaels, 2005; Malovichko and Rigby, 2022; Martínez-Martínez et al., 2016b; Mutlib et al., 2016; Nakayama et al., 2021; Roohezamin et al., 2022; Serra et al., 2017; Wu and Che, 2021; Zhou et al., 2025).

The change in velocity can also be used as an indicator to quantify the density of cracks formed in a rockmass. There exists a number of models which predict change in elastic properties of rocks due to formation of cracks (Guéguen and Schubnel, 2003; Paterson and Wong, 2005; Sayers and Kachanov, 1995). With increasing vertical stress, cracks form subparallel to the loading direction and assuming them to penny-shaped, we can use the formulation proposed by (Kachanov et al., 1993) (eq. 2) to calculate crack density from effective Young's modulus

$$\frac{E_{0dyn}}{E^*_{xdyn}} = 1 + \frac{16\left(1-\nu_0^2\right)}{3}\frac{\delta}{1+\delta}\varepsilon \tag{2}$$

where E_0 and ν_0 are the Young's modulus and Poisson's ratio of the solid matrix, respectively; Ex* is the effective Young's modulus along the x axis; δ is a nondimensional number referred to as the fluid saturation parameter; and ε is crack density. For simplicity, this model assumes transversely isotropic medium and no interaction between the individual cracks. We ignore the fluid saturation parameters and assume $\delta/(1+\delta) \to 1$ in our case. We also assume that at max Vp and Vs, the coreplug resembles closest to the solid matrix, since all pores and cracks are assumed to be closed at that point and negligible new cracks may have formed in the system, hence E_{0dyn} is calculated at that point.

The density was considered same during the experiment since the amount of crack volume is negligible compared to the sample volume. ν is measured from Vp and Vs using the following expression (eq. 3)

$$\nu = \frac{\left(\frac{V_P}{V_S}\right)^2 - 2}{2\left(\frac{V_P}{V_S}\right)^2 - 2} \tag{3}$$

Fig. 14 indicate the change in crack volume throughout the experiment. In most cases we can see a gradual closing of cracks while the axial stress increases, followed by a rapid increase in crack volume before complete failure of the rockmass.

It is also interesting to observe that the onset of dilatancy is strongly dependent on the porosity of the plugs. It is worthwhile to mention that dilatancy in this case is simply assessed based on the dynamic YM calculated from the axial Vp and Vs. High porosity samples have onset of dilatancy at 75–78 % of peak axial stress, whereas for high porosity samples the onset of dilatancy is at around 82–86 % of peak axial stress (Fig. 14). The amount of crack formed pre-failure is also higher in high porosity samples compared to their low porosity counterpart.

5. Conclusion

In this study with a comprehensive experimental approach, we define the change in ultrasonic velocity and amplitude as a response to stress change and eventually propose a workflow which can be developed as a relatively low-cost forecasting and monitoring tool for stress change in subsurface reservoirs and also applies to monitoring health in engineered structures like foundations, bridges, dams, tunnels and underground mining projects.

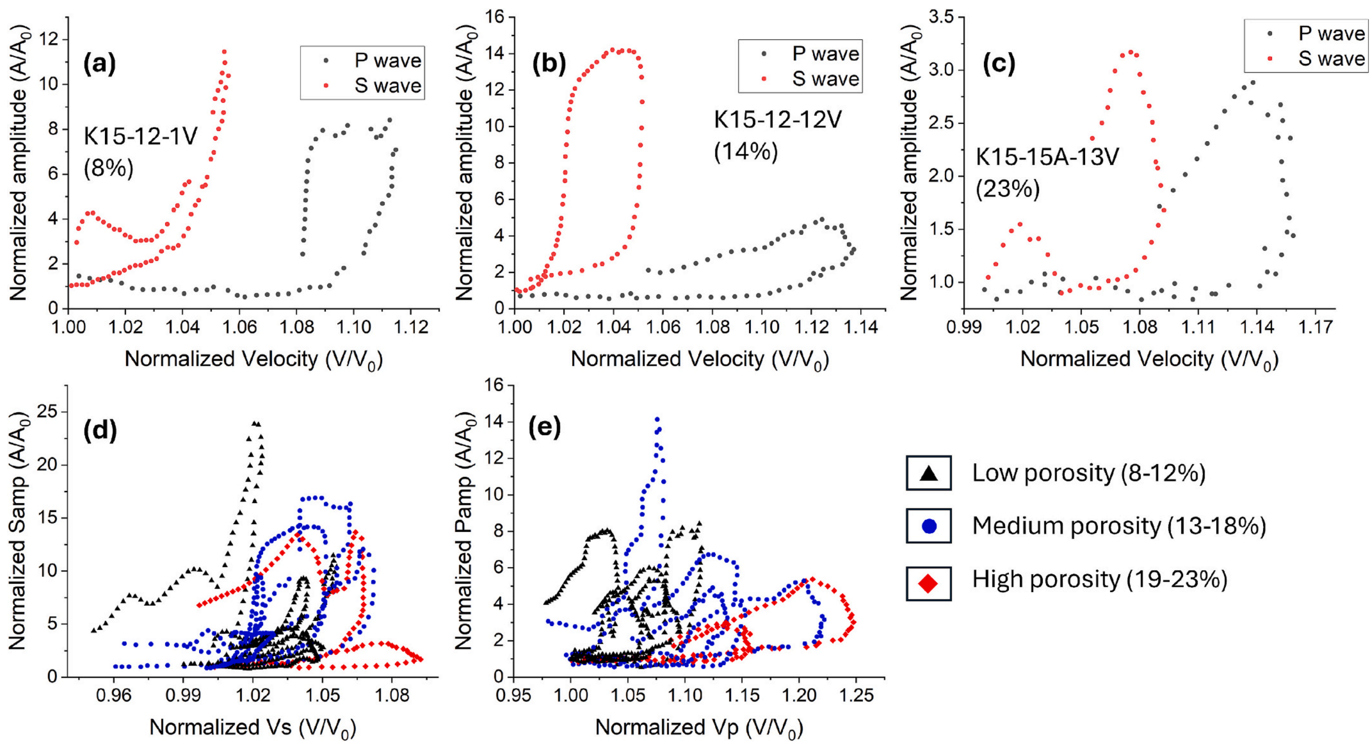

Fig. 11. Normalized velocity vs amplitude for a representative (a) low porosity, (b) medium porosity and (c) high porosity sample during triaxial failure experiment. (d) and (e) represent S wave and P wave velocity vs amplitude respectively for all tested samples. (For interpretation of the references to colour in this figure legend, the reader is referred to the web version of this article.)

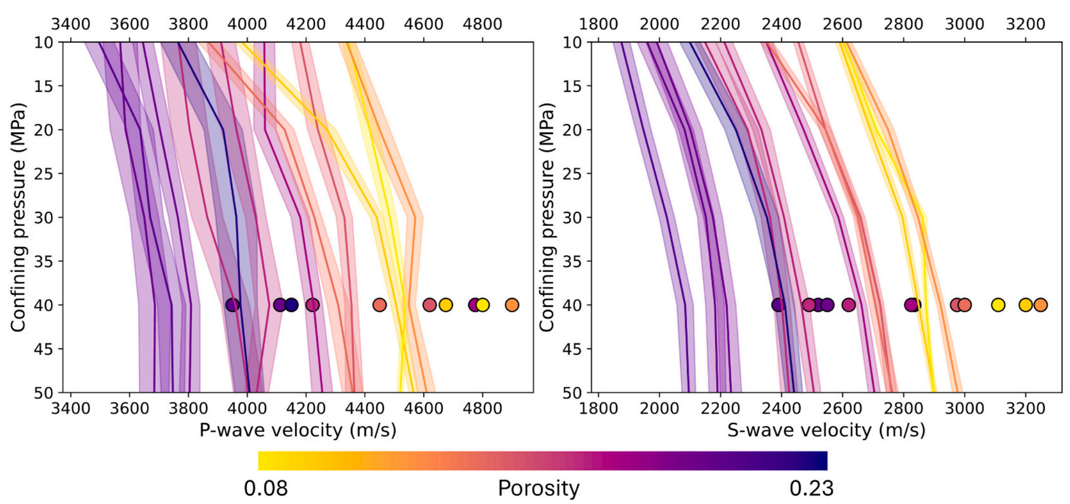

Fig. 12. Colorbars represent the velocity change from hydrostatic condition to 2× axial stress at each confining pressure for all samples where the colour indicates their porosity. The dots represent the maximum velocity of each specimen derived from failure experiments at 40 MPa confinement. (For interpretation of the references to colour in this figure legend, the reader is referred to the web version of this article.)

Experiments clearly indicate porosity having a strong inverse influence on ultrasonic velocity and mechanical properties. Compared to low porosity coreplugs, high porosity coreplugs show higher degree of change in velocity with increasing deviatoric stress which is caused by increased pore collapse. Increase in hydrostatic stress causes increase in velocity as the bulk density approaches maxima due to reduction in pore space, which also reduces the magnitude of change in velocity during elastic deformation.

Both Vp, Vs and their corresponding amplitude drops rapidly since the onset of plastic deformation. The temporal evolution of stress, ultrasonic velocity and amplitudes under constant deformation rate can be used to divide the stress profile in four distinct zones, which can be used for monitoring reservoir stress condition during fluid injection operation. Vp and Pamp shows synchronous response, whereas response of Samp precedes Vs. Relative change of Samp wrt Vs is found to be more sensitive during different stages of deformation compared to Pamp, especially for rocks with lower porosity. These observations iterate the requirement of both P and S wave measurement in the subsurface for accurate stress monitoring, specially where stress fluctuation is faster (near injection wellbore).

Sonic derived crack model indicates that rocks with higher porosity are more compliant, resulting in crack closure at lower relative stress

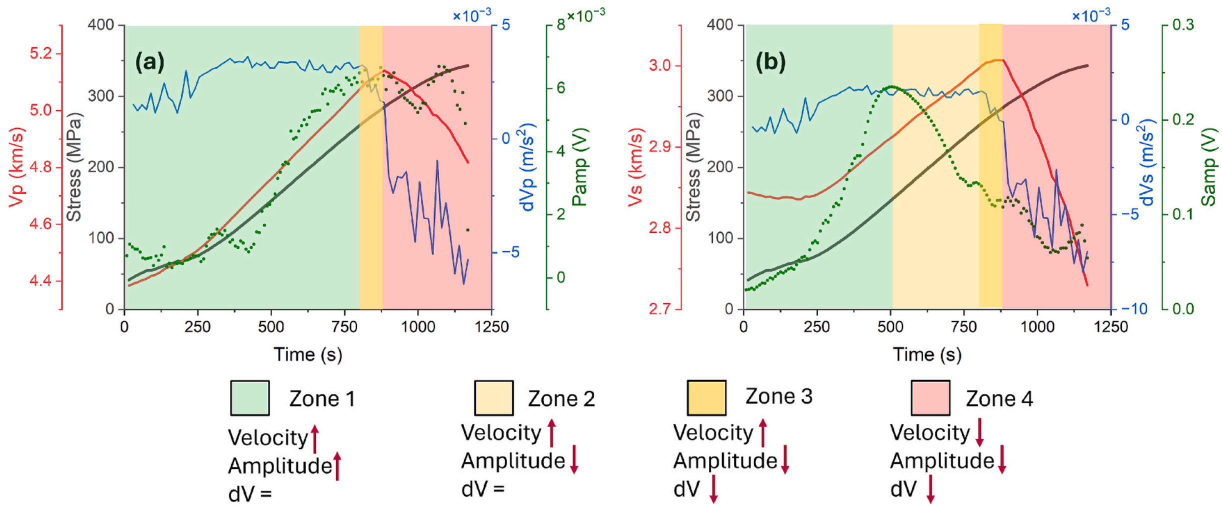

Fig. 13. An example of segregating different zones of deformation based on ultrasonic (a) P wave and (b) S wave velocity and amplitude responses. Here green (Zone 1) indicates safest stress regime and red (Zone 4) indicates most unsafe stress regime. (For interpretation of the references to colour in this figure legend, the reader is referred to the web version of this article.)

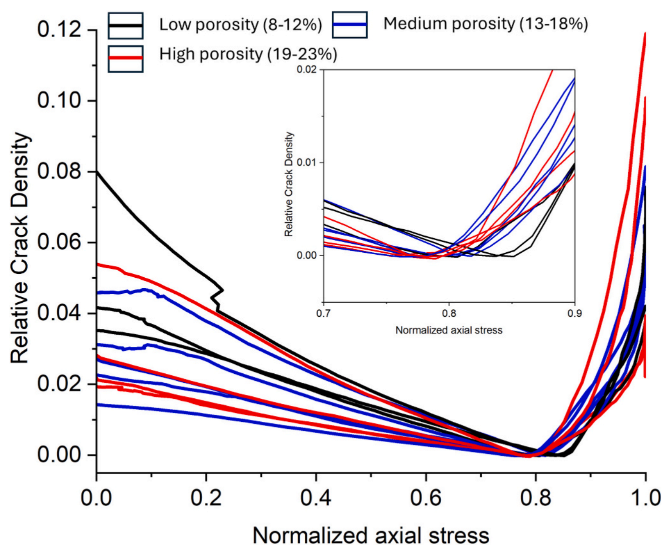

Fig. 14. Crack density vs normalized axial stress of the coreplugs grouped by their porosity based on Vp and Vs changes during deformation. (For interpretation of the references to colour in this figure legend, the reader is referred to the web version of this article.)

levels. Rocks with lower porosity are stiffer, requiring higher stress relative to peak stress to ensure crack closure. Conversely, with increasing stress, cracks accumulate at lower stress level relative to peak load in high-porosity rocks since the onset of plasticity. The correlation between stresses and sonic derived crack density model extends applicability of this study in other geoengineering projects, where other methods of deformation measurement are difficult to deploy, especially when timelapse monitoring is required. However, appropriate calibration of such models should be performed in lab-scale prior to field application.

The strength of this technique lies in its ability to not only monitor but also forecast critical stress change in a rockmass. This technique and its derivatives have the potential to emerge as a short-term and long-term monitoring solution for emerging CCS projects. However, the scope of use extends well beyond ensuring the safety of CCS operations and can be adapted for geothermal energy, UHS, or any other geoengineering application where precise monitoring of stress changes over time is required.

CRediT authorship contribution statement

Debanjan Chandra: Writing – original draft, Validation, Software, Methodology, Investigation, Formal analysis, Conceptualization. **Lujain Alghannam:** Writing – review & editing, Software, Formal analysis, Data curation. **Auke Barnhoorn:** Writing – review & editing, Supervision, Resources, Project administration, Investigation, Funding acquisition, Conceptualization.

Declaration of competing interest

The authors hereby declare no conflict of interest and that the work described has not been published previously, nor it is under consideration for publication elsewhere. The article's publication is approved by all authors before submission.

Acknowledgement

This publication has been produced with support from SHARP Storage (project no 327342). The SHARP project has been subsidized through ACT (EC Project no. 691712), by Rijksdienst voor Ondernemend Nederland (RVO). Marc Friebel, Jens van den Berg and Karel Heller are duly acknowledged for their technical support in sample preparation and setting up the experiments.

Data availability

Data will be made available on request.

References

Agofack, N., Lozovyi, S., Bauer, A., 2018. Effect of CO2 on P- and S-wave velocities at seismic and ultrasonic frequencies. Int. J. Greenh. Gas Control 78, 388–399. https://doi.org/10.1016/J.IJGGC.2018.09.010.

Al Shafloot, T., Kohli, A., Kim, T.W., Kovscek, A.R., 2024. Impact of supercritical carbon dioxide on the frictional strength of and the transport through thin cracks in shale. J. Rock Mech. Geotech. Eng. https://doi.org/10.1016/J.JRMGE.2023.12.021.

Al-Shayea, N.A., 2001. The combined effect of clay and moisture content on the behavior of remolded unsaturated soils. Eng. Geol. 62, 319–342. https://doi.org/10.1016/S0013-7952(01)00032-1.

Ashby, M.F., Hallam, S.D., 1986. The failure of brittle solids containing small cracks under compressive stress states. Acta Metall. 34, 497–510. https://doi.org/10.1016/0001-6160(86)90086-6.

Barnhoorn, A., Verheij, J., Frehner, M., Zhubayev, A., Houben, M., 2018. Experimental identification of the transition from elasticity to inelasticity from ultrasonic attenuation analyses. Geophysics 83, MR221–MR229. https://doi.org/10.1190/GEO2017-0534.1/ASSET/IMAGES/LARGE/FIGURE7.JPEG.

Brotons, V., Tomás, R., Ivorra, S., Grediaga, A., Martínez-Martínez, J., Benavente, D., Gómez-Heras, M., 2016. Improved correlation between the static and dynamic elastic modulus of different types of rocks. Mater. Struct. 49, 3021–3037. https://doi.org/10.1617/S11527-015-0702-7/FIGURES/11.

Buijze, L., Van Bijsterveldt, L., Cremer, H., Paap, B., Veldkamp, H., Wassing, B.B.T., Van Wees, J.D., Van Yperen, G.C.N., Ter Heege, J.H., 2019. Review of induced seismicity in geothermal systems worldwide and implications for geothermal systems in the Netherlands. Neth. J. Geosci. 98, e13. https://doi.org/10.1017/NJG.2019.6.

Bump, A.P., Hovorka, S.D., 2023. Minimizing exposure to legacy wells and avoiding conflict between storage projects: Exploring area of review as a screening tool. Int. J. Greenh. Gas Control 129, 103967. https://doi.org/10.1016/J.IJGGC.2023.103967.

Bump, A.P., Hovorka, S.D., 2024. Pressure space: the key subsurface commodity for CCS. Int. J. Greenh. Gas Control 136, 104174. https://doi.org/10.1016/J.IJGGC.2024.104174.

Cao, W., Shi, J.Q., Durucan, S., Korre, A., 2021. Evaluation of shear slip stress transfer mechanism for induced microseismicity at in Salah CO2 storage site. Int. J. Greenh. Gas Control 107, 103302. https://doi.org/10.1016/J.IJGGC.2021.103302.

Caspari, E., Müller, T.M., Gurevich, B., 2011. Time-lapse sonic logs reveal patchy CO2 saturation in-situ. Geophys. Res. Lett. 38. https://doi.org/10.1029/2011GL046959.

Chandra, D., Barnhoorn, A., 2025. Ultrasonic Response of a Brine-saturated Reservoir Rock During Coupled Stress and Fluid Perturbation During Liquid-CO2 Injection. Int. J. Greenh. Gas Control. 147C, 104498. https://doi.org/10.1016/j.ijggc.2025.104498.

Che, A., Tang, Z., Feng, S., 2015. An elastic-wave-based full-wavefield imaging method for investigating defects in a high-speed railway under-track structure. Soil Dyn. Earthq. Eng. 77, 299–308. https://doi.org/10.1016/J.SOILDYN.2015.06.005.

Chen, H., Yang, S., Huan, K., Li, F., Huang, W., Zheng, A., Zhang, X., 2013. Experimental study on monitoring CO2 sequestration by conjoint analysis of the P-wave velocity and amplitude. Environ. Sci. Technol. 47, 10071–10077. https://doi.org/10.1021/ES4017409/ASSET/IMAGES/LARGE/ES-2013-017409_0009.JPEG.

Cheng, Y., Liu, W., Xu, T., Zhang, Y., Zhang, X., Xing, Y., Feng, B., Xia, Y., 2023. Seismicity induced by geological CO2 storage: a review. Earth Sci. Rev. 239, 104369. https://doi.org/10.1016/J.EARSCIREV.2023.104369.

Choi, J.C., Skurtveit, E., Huynh, K.D.V., Grande, L., 2023. Uncertainty of stress path in fault stability assessment during CO2 injection: comparing smeaheia 3D geomechanics model with analytical approaches. Int. J. Greenh. Gas Control 125, 103881. https://doi.org/10.1016/J.IJGGC.2023.103881.

CLIMIT, 2020. Induced-seismicity geomechanics for controlled CO2 storage in the North Sea (IGCCS), CLIMIT project final report KPN-268520/E20.

Cornelio, C., Violay, M., 2020. Parametric analysis of the elastohydrodynamic lubrication efficiency on induced seismicity. Geophys. J. Int. 222, 517–525. https://doi.org/10.1093/GJI/GGAA180.

De Jager, J., Geluk, M.C., 2007. Petroleum geology. In: Wong, T., Batjes, D., de Jager, J. (Eds.), Geology of the Netherlands. Royal Netherlands Academy of Arts and Sciences (KNAW), Amsterdam, pp. 241–264.

Delle Piane, C., Sarout, J., 2016. Effects of water and supercritical CO2 on the mechanical and elastic properties of Berea sandstone. Int. J. Greenh. Gas Control 55, 209–220. https://doi.org/10.1016/J.IJGGC.2016.06.001.

Deng, Z., Huang, M., Wan, N., Zhang, J., 2023. The current development of structural health monitoring for bridges: a review. Buildings 13, 1360. https://doi.org/10.3390/BUILDINGS13061360.

El-Husseiny, A., Vega, S., Nizamuddin, S., 2019. The effect of pore structure complexity and saturation history on the variations of acoustic velocity as function of brine and oil saturation in carbonates. J. Pet. Sci. Eng. 179, 180–191. https://doi.org/10.1016/J.PETROL.2019.04.019.

Ersoy, H., Karahan, M., Babacan, A.E., Sünnetci, M.O., 2019. A new approach to the effect of sample dimensions and measurement techniques on ultrasonic wave velocity. Eng. Geol. 251, 63–70. https://doi.org/10.1016/J.ENGGEO.2019.02.011.

Falcon-Suarez, I., North, L., Amalokwu, K., Best, A., 2016. Integrated geophysical and hydromechanical assessment for CO2 storage: shallow low permeable reservoir sandstones. Geophys. Prospect. 64, 828–847. https://doi.org/10.1111/1365-2478.12396/CITE/REFWORKS.

Falcon-Suarez, I., Papageorgiou, G., Chadwick, A., North, L., Best, A.I., Chapman, M., 2018. CO2-brine flow-through on an Utsira Sand core sample: experimental and modelling. Implications for the Sleipner storage field. Int. J. Greenh. Gas Control 68, 236–246. https://doi.org/10.1016/J.IJGGC.2017.11.019.

Falcon-Suarez, I.H., Papageorgiou, G., Jin, Z., Muñoz-Ibáñez, A., Chapman, M., Best, A.I., 2020. CO2-brine substitution effects on ultrasonic wave propagation through sandstone with oblique fractures. Geophys. Res. Lett. 47. https://doi.org/10.1029/2020GL088439 e2020GL088439.

Falls, S.D., Young, R.P., 1998. Acoustic emission and ultrasonic-velocity methods used to characterise the excavation disturbance associated with deep tunnels in hard rock. Tectonophysics 289, 1–15. https://doi.org/10.1016/S0040-1951(97)00303-X.

Fjær, E., 2009. Static and dynamic moduli of a weak sandstone. Geophysics 74. https://doi.org/10.1190/1.3052113/ASSET/IMAGES/LARGE/006902GPY18.JPEG.

Fortin, J., Schubnel, A., Guéguen, Y., 2005. Elastic wave velocities and permeability evolution during compaction of Bleurswiller sandstone. Int. J. Rock Mech. Min. Sci. 42, 873–889. https://doi.org/10.1016/J.IJRMMS.2005.05.002.

Fortin, J., Stanchits, S., Vinciguerra, S., Guéguen, Y., 2011. Influence of thermal and mechanical cracks on permeability and elastic wave velocities in a basalt from Mt. Etna volcano subjected to elevated pressure. Tectonophysics 503, 60–74. https://doi.org/10.1016/J.TECTO.2010.09.028.

Gasperikova, E., Appriou, D., Bonneville, A., Feng, Z., Huang, L., Gao, K., Yang, X., Daley, T., 2022. Sensitivity of geophysical techniques for monitoring secondary CO2 storage plumes. Int. J. Greenh. Gas Control 114, 103585. https://doi.org/10.1016/J.IJGGC.2022.103585.

Gassman, F., 1951. Uber die elastizitat poroser medien. Vierteljahrsschrift der Naturforschenden Gesellschaft in Zurich 96, 1–23.

Geluk, M.C., Röhling, H.G., 1997. High-resolution sequence stratigraphy of the Lower Triassic 'Buntsandstein' in the Netherlands and northwestern Germany. Geol. Mijnb. 3 (76), 227–246. https://doi.org/10.1023/A:1003062521373.

Ghosh, R., Sen, M.K., 2012. Predicting subsurface CO2 movement: from laboratory to field scale. Geophysics 77. https://doi.org/10.1190/GEO2011-0224.1/ASSET/IMAGES/LARGE/FIGURE10.JPEG.

Gladwin, M.T., 1982. Ultrasonic stess monitoring in underground mining. Int. J. Rock Mech. Min. Sci. Geomech. Abstr. 19, 221–228. https://doi.org/10.1016/0148-9062(82)90220-0.

Goertz-Allmann, B.P., Kühn, D., Oye, V., Bohloli, B., Aker, E., 2014. Combining microseismic and geomechanical observations to interpret storage integrity at the in Salah CCS site. Geophys. J. Int. 198, 447–461. https://doi.org/10.1093/GJI/GGU010.

Gonzalez, A., Mabon, L., Agarwal, A., 2021. Who wants North Sea CCS, and why? Assessing differences in opinion between oil and gas industry respondents and wider energy and environmental stakeholders. Int. J. Greenh. Gas Control 106, 103288. https://doi.org/10.1016/J.IJGGC.2021.103288.

Grande, L., Griffiths, L., Park, J., Skurtveit, E., Thompson, N., 2024. Cooling-induced geomechanical response of North Sea reservoirs, and relevance for CO2 storage monitoring. Int. J. Greenh. Gas Control 138, 104228. https://doi.org/10.1016/J.IJGGC.2024.104228.

Griffiths, L., Heap, M.J., Xu, T., Chen, C. Feng, Baud, P., 2017. The influence of pore geometry and orientation on the strength and stiffness of porous rock. J. Struct. Geol. 96, 149–160. https://doi.org/10.1016/J.JSG.2017.02.006.

Griffiths, L., Dautriat, J., Park, J., Rodriguez, I.V., Iranpour, K., Sauvin, G., Sarout, J., Grande, L., Oye, V., Soldal, M., Dewhurst, D.N., Mondol, N.H., Choi, J.C., 2021. The Influence of Super-Critical CO2 Saturation on the Mechanical and Failure Properties of a North Sea Reservoir Sandstone Analogue. 15th Greenhouse Gas Control Technologies Conference 2021, GHGT 2021. https://doi.org/10.2139/SSRN.3818808.

Grude, S., Landrø, M., Dvorkin, J., 2014. Pressure effects caused by CO2 injection in the Tubåen Fm., the Snøhvit field. Int. J. Greenh. Gas Control 27, 178–187. https://doi.org/10.1016/J.IJGGC.2014.05.013.

Guéguen, Y., Schubnel, A., 2003. Elastic wave velocities and permeability of cracked rocks. Tectonophysics 370, 163–176. https://doi.org/10.1016/S0040-1951(03)00184-7.

Guo, M.Q., Fu, L.Y., Ba, J., 2009. Comparison of stress-associated coda attenuation and intrinsic attenuation from ultrasonic measurements. Geophys. J. Int. 178, 447–456. https://doi.org/10.1111/J.1365-246X.2009.04159.X/3/178-1-447-FIG 009.JPEG.

Hamada, G., Joseph, V., 2020. Developed correlations between sound wave velocity and porosity, permeability and mechanical properties of sandstone core samples. Petroleum Res. 5, 326–338. https://doi.org/10.1016/J.PTLRS.2020.07.001.

Hamdi, E., Lafhaj, Z., 2013. Microcracking based rock classification using ultrasonic and porosity parameters and multivariate analysis methods. Eng. Geol. 167, 27–36. https://doi.org/10.1016/J.ENGGEO.2013.10.008.

Hansen, O., Gilding, D., Nazarian, B., Osdal, B., Ringrose, P., Kristoffersen, J.B., Eiken, O., Hansen, H., 2013. Snøhvit: the history of Injecting and Storing 1 Mt CO2 in the Fluvial Tubåen Fm. Energy Procedia 37, 3565–3573. https://doi.org/10.1016/J.EGYPRO.2013.06.249.

Hart, D.J., Wang, H.F., 1995. Laboratory measurements of a complete set of poroelastic moduli for Berea sandstone and Indiana limestone. J. Geophys. Res. Solid Earth 100, 17741–17751. https://doi.org/10.1029/95JB01242.

He, W., Chen, Z., Shi, H., Liu, C., Li, S., 2021. Prediction of acoustic wave velocities by incorporating effects of water saturation and effective pressure. Eng. Geol. 280, 105890. https://doi.org/10.1016/J.ENGGEO.2020.105890.

Janssen, M.T.G., Barnhoorn, A., Draganov, D., Wolf, K.H.A.A., Durucan, S., 2021. Seismic velocity characterisation of geothermal reservoir rocks for CO2 storage performance assessment. Appl. Sci. (Switzerland) 11, 3641. https://doi.org/10.3390/APP11083641/S1.

Kachanov, M., Hutchinson, J.E., Wu, T.Y.T., 1993. Advances in Applied Mechanics. Elsevier.

King, M.S., 1969. Static and dynamic elastic moduli of rocks under pressure. In: The 11th U.S. Symposium on Rock Mechanics (USRMS). OnePetro, Berkeley.

Le Ding, Q., Song, S.B., 2016. Experimental investigation of the relationship between the P-wave velocity and the mechanical properties of damaged sandstone. Adv. Mater. Sci. Eng. 2016, 7654234. https://doi.org/10.1155/2016/7654234.

Lee, H., Romero, J., Core Writing Team, 2023. IPCC, 2023: Climate Change 2023: Synthesis Report. Contribution of Working Groups I, II and III to the Sixth Assessment Report of the Intergovernmental Panel on Climate Change. Geneva, Switzerland.

Li, K., Pluymakers, A.M.H., 2024. Effects of thermal shocks on integrity of existing and newly-designed sealants for CCS applications. Int. J. Greenh. Gas Control 133, 104103. https://doi.org/10.1016/J.IJGGC.2024.104103.

Li, Y., Zhu, Z., 2012. Study on the velocity of P waves across a single joint based on fractal and damage theory. Eng. Geol. 151, 82–88. https://doi.org/10.1016/J.ENGGEO.2012.09.006.

Li, L., Ma, J.F., Wang, H.F., Tan, M.Y., Cui, S.L., Zhang, Y.Y., Qu, Z.P., 2017. Shear wave velocity prediction during CO2-EOR and sequestration in the Gao89 well block of the Shengli Oilfield. Appl. Geophys. 14, 372–380. https://doi.org/10.1007/S11770-017-0638-5/METRICS.

Li, Guoliang, Li, Guanfang, Wang, Y., Qi, S., Yang, J., 2020. A rock physics model for estimating elastic properties of upper Ordovician-lower Silurian mudrocks in the Sichuan Basin, China. Eng. Geol. 266, 105460. https://doi.org/10.1016/J.ENGGEO.2019.105460.

Li, Z., Zuo, J., Sun, Y., Shi, Y., Ma, Z., 2022. Investigation on sandstone wave velocity variation and the stress response of pore structure. Bull. Eng. Geol. Environ. 81, 1–17. https://doi.org/10.1007/S10064-022-02723-X/FIGURES/14.

Lu, Y., Michaels, J.E., 2005. A methodology for structural health monitoring with diffuse ultrasonic waves in the presence of temperature variations. Ultrasonics 43, 717–731. https://doi.org/10.1016/J.ULTRAS.2005.05.001.

Lund, J.W., Toth, A.N., 2021. Direct utilization of geothermal energy 2020 worldwide review. Geothermics 90, 101915. https://doi.org/10.1016/J.GEOTHERMICS.2020.101915.

Majer, E.L., Baria, R., Stark, M., Oates, S., Bommer, J., Smith, B., Asanuma, H., 2007. Induced seismicity associated with enhanced geothermal systems. Geothermics 36, 185–222. https://doi.org/10.1016/J.GEOTHERMICS.2007.03.003.

Malovichko, D., Rigby, A., 2022. Description of Seismic Sources in Underground Mines: Dynamic Stress Fracturing around Tunnels and Strainbursting. ArXiv.

Martínez-Martínez, J., Benavente, D., García del Cura, M.A., 2007. Petrographic quantification of brecciated rocks by image analysis. Application to the interpretation of elastic wave velocities. Eng. Geol. 90, 41–54. https://doi.org/10.1016/J.ENGGEO.2006.12.002.

Martínez-Martínez, J., Benavente, D., García-del-Cura, M.A., 2011. Spatial attenuation: the most sensitive ultrasonic parameter for detecting petrographic features and decay processes in carbonate rocks. Eng. Geol. 119, 84–95. https://doi.org/10.1016/J.ENGGEO.2011.02.002.

Martínez-Martínez, J., Fusi, N., Galiana-Merino, J.J., Benavente, D., Crosta, G.B., 2016a. Ultrasonic and X-ray computed tomography characterization of progressive fracture damage in low-porous carbonate rocks. Eng. Geol. 200, 47–57. https://doi.org/10.1016/J.ENGGEO.2015.11.009.

Martínez-Martínez, J., Fusi, N., Galiana-Merino, J.J., Benavente, D., Crosta, G.B., 2016b. Ultrasonic and X-ray computed tomography characterization of progressive fracture damage in low-porous carbonate rocks. Eng. Geol. 200, 47–57. https://doi.org/10.1016/J.ENGGEO.2015.11.009.

Mavko, G., Mukerji, T., Godfrey, N., 2012. Predicting stress-induced velocity anisotropy in rocks, 60, 1081–1087. https://doi.org/10.1190/1.1443836.

Mayr, S.I., Burkhardt, H., 2006. Ultrasonic properties of sedimentary rocks: effect of pressure, saturation, frequency and microcracks. Geophys. J. Int. 164, 246–258. https://doi.org/10.1111/J.1365-246X.2005.02826.X/2/M_164-1-246-EQ015.GIF.

Müller, N., Ramakrishnan, T.S., Boyd, A., Sakruai, S., 2007. Seismic monitoring and modelling of supercritical CO2 injection into a water-saturated sandstone: Interpretation of P-wave velocity data. Int. J. Greenh. Gas Control 1, 473–480. https://doi.org/10.1016/S1750-5836(07)00013-8.

Murdoch, L.C., Germanovich, L.N., DeWolf, S.J., Moysey, S.M.J., Hanna, A.C., Kim, S., Duncan, R.G., 2020. Feasibility of using in situ deformation to monitor CO2 storage. Int. J. Greenh. Gas Control 93, 102853. https://doi.org/10.1016/J.IJGGC.2019.102853.

Mutlib, N.K., Baharom, S. Bin, El-Shafie, A., Nuawi, M.Z., 2016. Ultrasonic health monitoring in structural engineering: buildings and bridges. Struct. Control. Health Monit. 23, 409–422. https://doi.org/10.1002/STC.1800.

Myer, L.R., Daley, T.M., 2011. Elements of a best practices approach to induced seismicity in geologic storage. Energy Procedia 4, 3707–3713. https://doi.org/10.1016/J.EGYPRO.2011.02.303.

Naderloo, M., Ramesh Kumar, K., Hernandez, E., Hajibeygi, H., Barnhoorn, A., 2023. Experimental and numerical investigation of sandstone deformation under cycling loading relevant for underground energy storage. J Energy Storage 64, 107198. https://doi.org/10.1016/J.EST.2023.107198.

Nakajima, T., Wang, L., Xue, Z., 2019. Utilization of wave attenuation in the time-lapse sonic logging at the Nagaoka site for a near well monitoring of CO2 migration. Int. J. Greenh. Gas Control 88, 342–352. https://doi.org/10.1016/J.IJGGC.2019.06.022.

Nakayama, M., Kawakata, H., Hirano, S., Doi, I., 2021. Development of a laboratory monitoring system for elastic waves transmitted through sand under dry and nearly saturated conditions. Earth Planets Space 73, 1–12. https://doi.org/10.1186/S40623-020-01346-4/FIGURES/8.

Nasseri, M.H.B., Schubnel, A., Benson, P.M., Young, R.P., 2009. Common evolution of mechanical and transport properties in thermally cracked westerly granite at elevated hydrostatic pressure. Pure Appl. Geophys. 166, 927–948. https://doi.org/10.1007/S00024-009-0485-2/METRICS.

Nefeslioglu, H.A., 2013. Evaluation of geo-mechanical properties of very weak and weak rock materials by using non-destructive techniques: ultrasonic pulse velocity measurements and reflectance spectroscopy. Eng. Geol. 160, 8–20. https://doi.org/10.1016/J.ENGGEO.2013.03.023.

Nooraiepour, M., Bohloli, B., Park, J., Sauvin, G., Skurtveit, E., Mondol, N.H., 2017. Effect of brine-CO2 fracture flow on velocity and electrical resistivity of naturally fractured tight sandstones, 83, WA37–WA48. https://doi.org/10.1190/GEO2017-0077.1.

Nooraiepour, M., Bohloli, B., Park, J., Sauvin, G., Skurtveit, E., Mondol, N.H., 2018. Effect of brine-CO2 fracture flow on velocity and electrical resistivity of naturally fractured tight sandstones. Geophysics 83, WA37–WA48. https://doi.org/10.1190/GEO2017-0077.1/ASSET/IMAGES/LARGE/FIGURE10.JPEG.

Palchik, V., 1999. Influence of porosity and elastic modulus on uniaxial compressive strength in soft brittle porous sandstones. Rock Mech. Rock. Eng. 32, 303–309. https://doi.org/10.1007/S006030050050/METRICS.

Park, J., Griffiths, L., Dautriat, J., Grande, L., Rodriguez, I.V., Iranpour, K., Bjørnarå, T.I., Moreno, H.M., Mondol, N.H., Sauvin, G., Sarout, J., Soldal, M., Oye, V., Dewhurst, D. N., Choi, J.C., Best, A.I., 2022. Induced-seismicity geomechanics for controlled CO2 storage in the North Sea (IGCCS). Int. J. Greenh. Gas Control 115, 103614. https://doi.org/10.1016/J.IJGGC.2022.103614.

Paterson, M.S., Wong, T.F., 2005. Experimental rock deformation - The brittle field. In: Experimental Rock Deformation - The Brittle Field. Springer Berlin Heidelberg. https://doi.org/10.1007/B137431/COVER.

Pijnenburg, R.P.J., Verberne, B.A., Hangx, S.J.T., Spiers, C.J., 2018. Deformation behavior of sandstones from the seismogenic Groningen gas field: role of inelastic versus elastic mechanisms. J. Geophys. Res. Solid Earth 123, 5532–5558. https://doi.org/10.1029/2018JB015673.

Pijnenburg, R.P.J., Verberne, B.A., Hangx, S.J.T., Spiers, C.J., 2019. Inelastic deformation of the Slochteren sandstone: stress-strain relations and implications for induced seismicity in the Groningen gas field. J. Geophys. Res. Solid Earth 124, 5254–5282. https://doi.org/10.1029/2019JB017366.

Polak, Amir, Elsworth, Derek, Liu, Jishan, Grader, Abraham S., Polak, A., Elsworth, D., Liu, J., Grader, A.S., 2004. Spontaneous switching of permeability changes in a limestone fracture with net dissolution. Water Resour. Res. 40, 3502. https://doi.org/10.1029/2003WR002717.

Qi, Y., Ju, Y., Yu, K., Meng, S., Qiao, P., 2022. The effect of grain size, porosity and mineralogy on the compressive strength of tight sandstones: a case study from the eastern Ordos Basin, China. J. Pet. Sci. Eng. 208, 109461. https://doi.org/10.1016/J.PETROL.2021.109461.

Raji, N., Consoli, C., Steyn, M., Havercroft, I., 2023. The global status of carbon capture and storage: ambition to action. APPEA J. 63, S423–S427. https://doi.org/10.1071/AJ22138.

Ramesh Kumar, K., Honorio, H., Chandra, D., Lesueur, M., Hajibeygi, H., 2023. Comprehensive review of geomechanics of underground hydrogen storage in depleted reservoirs and salt caverns. J Energy Storage 73, 108912. https://doi.org/10.1016/J.EST.2023.108912.

Rice-Birchall, E., Faulkner, D.R., Bedford, J.D., 2022. The effect of grain size and porosity on the nature of compaction localisation in high-porosity sandstone. J. Struct. Geol. 164, 104740. https://doi.org/10.1016/J.JSG.2022.104740.

Ringrose, P.S., Mathieson, A.S., Wright, I.W., Selama, F., Hansen, O., Bissell, R., Saoula, N., Midgley, J., 2013. The In Salah CO2 storage project: lessons learned and knowledge transfer. Energy Procedia 37, 6226–6236. https://doi.org/10.1016/J.EGYPRO.2013.06.551.

Roohezamin, A., Kalatehjari, R., Hajihassani, M., Kharghani, M., Dias, D., 2022. Investigation of acoustic waves behavior of an underground tunnel in a multilayer soil. Sci. Rep. 12, 1–15. https://doi.org/10.1038/S41598-022-16991-W;SUBJMETA=166,2151,2809,639,704,986;KWRD=CIVIL+ENGINEERING,ENGINEERING,GEOPHYSICS.

Rossi, M., Wisén, R., Vignoli, G., Coni, M., 2022. Assessment of distributed acoustic sensing (DAS) performance for geotechnical applications. Eng. Geol. 306, 106729. https://doi.org/10.1016/J.ENGGEO.2022.106729.

Rutqvist, J., Rinaldi, A.P., Cappa, F., Jeanne, P., Mazzoldi, A., Urpi, L., Guglielmi, Y., Vilarrasa, V., 2016. Fault activation and induced seismicity in geological carbon storage – Lessons learned from recent modeling studies. J. Rock Mech. Geotech. Eng. 8, 789–804. https://doi.org/10.1016/j.jrmge.2016.09.001.

Sambo, C., Dudun, A., Samuel, S.A., Esenenjor, P., Muhammed, N.S., Haq, B., 2022. A review on worldwide underground hydrogen storage operating and potential fields. Int. J. Hydrog. Energy 47, 22840–22880. https://doi.org/10.1016/J.IJHYDENE.2022.05.126.

Sayers, C.M., 2002. Stress-dependent elastic anisotropy of sandstones. Geophys. Prospect. 50, 85–95. https://doi.org/10.1046/J.1365-2478.2002.00289.X/CITE/REFWORKS.

Sayers, C.M., Kachanov, M., 1995. Microcrack-induced elastic wave anisotropy of brittle rocks. J. Geophys. Res. Solid Earth 100, 4149–4156. https://doi.org/10.1029/94JB03134.

Serra, M., Festa, G., Vassallo, M., Zollo, A., Quattrone, A., Ceravolo, R., 2017. Damage detection in elastic properties of masonry bridges using coda wave interferometry. Struct. Control. Health Monit. 24, e1976. https://doi.org/10.1002/STC.1976;WGROUP:STRING:PUBLICATION.

Shahsavari, M.H., Shakiba, M., 2022. An experimental insight into the influence of sand grain size distribution on the petrophysical and geomechanical properties of artificially made sandstones. J. Pet. Sci. Eng. 215, 110632. https://doi.org/10.1016/J.PETROL.2022.110632.

Shalev, E., Lyakhovsky, V., Ougier-Simonin, A., Hamiel, Y., Zhu, W., 2014. Inelastic compaction, dilation and hysteresis of sandstones under hydrostatic conditions. Geophys. J. Int. 197, 920–925. https://doi.org/10.1093/GJI/GGU052.

Sorbier, A., 2024. Offshore CCS: A North Sea Perspective from the Aramis Project 2024, pp. 1–5. https://doi.org/10.3997/2214-4609.2024101731.

Sujatono, S., Wijaya, A.E., 2022. The influence of quartz content on modulus of elasticity and Poisson's ratio in quartz sandstone. Bull. Eng. Geol. Environ. 81, 1–11. https://doi.org/10.1007/S10064-022-02798-6/TABLES/4.

Sun, Y., Liu, J., Xue, Z., Li, Q., Fan, C., Zhang, X., 2021. A critical review of distributed fiber optic sensing for real-time monitoring geologic CO2 sequestration. J. Nat. Gas Sci. Eng. 88, 103751. https://doi.org/10.1016/J.JNGSE.2020.103751.

Swennenhuis, F., Mabon, L., Flach, T.A., de Coninck, H., 2020. What role for CCS in delivering just transitions? An evaluation in the North Sea region. Int. J. Greenh. Gas Control 94, 102903. https://doi.org/10.1016/J.IJGGC.2019.102903.

Tutuncu, A.N., Podio, A.L., Sharma, M.M., 1998. Nonlinear viscoelastic behavior of sedimentary rocks, Part II: hysteresis effects and influence of type of fluid on elastic moduli. Geophysics 63, 195–203. https://doi.org/10.1190/1.1444313;PAGEGROUP:STRING:PUBLICATION.

Veltmeijer, A., Naderloo, M., Barnhoorn, A., 2024. Precursors to rock failure in the laboratory using ultrasonic monitoring methods. Geomech. Geophys. Geo-Energy Geo-Resour. 10, 1–15. https://doi.org/10.1007/S40948-024-00812-7/FIGURES/9.

Vilarrasa, V., Laloui, L., 2016. Impacts of thermally induced stresses on fracture stability during geological storage of CO2. Energy Procedia 86, 411–419. https://doi.org/10.1016/J.EGYPRO.2016.01.042.

Vilarrasa, V., Rutqvist, J., 2017. Thermal effects on geologic carbon storage. Earth Sci. Rev. 165, 245–256. https://doi.org/10.1016/J.EARSCIREV.2016.12.011.

Vilarrasa, V., Olivella, S., Carrera, J., Rutqvist, J., 2014. Long term impacts of cold CO2 injection on the caprock integrity. Int. J. Greenh. Gas Control 24, 1–13. https://doi.org/10.1016/J.IJGGC.2014.02.016.

Wang, Y., Han, D.H., Li, H., Zhao, L., Ren, J., Zhang, Y., 2020. A comparative study of the stress-dependence of dynamic and static moduli for sandstones. Geophysics 85, MR179–MR190. https://doi.org/10.1190/GEO2019-0335.1.

Wei, W., Fu, L.Y., 2014. Monte Carlo simulation of stress-associated scattering attenuation from laboratory ultrasonic measurements. Bull. Seismol. Soc. Am. 104, 931–943. https://doi.org/10.1785/0120130082.

White, J.A., Foxall, W., 2016. Assessing induced seismicity risk at CO2 storage projects: recent progress and remaining challenges. Int. J. Greenh. Gas Control 49, 413–424. https://doi.org/10.1016/J.IJGGC.2016.03.021.

White, D., Harris, K., Roach, L., Roberts, B., Worth, K., Stork, A., Nixon, C., Schmitt, D., Daley, T., Samson, C., 2017. Monitoring results after 36 Ktonnes of deep CO2 injection at the aquistore CO2 storage site, Saskatchewan, Canada. Energy Procedia 114, 4056–4061. https://doi.org/10.1016/J.EGYPRO.2017.03.1546.

Will, R., Smith, V., Leetaru, H.E., Freiburg, J.T., Lee, D.W., 2014. Microseismic monitoring, event occurrence, and the relationship to subsurface geology. Energy Procedia 63, 4424–4436. https://doi.org/10.1016/J.EGYPRO.2014.11.478.

Williams, M., Ziegler, M., Schennen, S., Loew, S., 2022. Evolution of excavation damaged zones in Opalinus Clay shale inferred from seismic investigations. Eng. Geol. 299, 106528. https://doi.org/10.1016/J.ENGGEO.2022.106528.

Wu, P., Che, A., 2021. Spatiotemporal monitoring and evaluation method for sand-filling of immersed tube tunnel foundation. Appl. Sci. 11, 1084. https://doi.org/10.3390/APP11031084.

Xia, K., Chen, C., Wang, T., Zheng, Y., Wang, Y., 2022. Estimating the geological strength index and disturbance factor in the Hoek–Brown criterion using the acoustic wave velocity in the rock mass. Eng. Geol. 306, 106745. https://doi.org/10.1016/J.ENGGEO.2022.106745.

Xu, C., Lin, C., Kang, Y., You, L., 2018. An experimental study on porosity and permeability stress-sensitive behavior of sandstone under hydrostatic compression: characteristics, mechanisms and controlling factors. Rock Mech. Rock. Eng. 51, 2321–2338. https://doi.org/10.1007/S00603-018-1481-6/FIGURES/14.

Xue, Z., Tanase, D., Watanabe, J., 2006. Estimation of CO2 saturation from time-lapse CO2 well logging in an onshore aquifer, Nagaoka, Japan. Explor. Geophys. 37, 19–29. https://doi.org/10.1071/EG06019.

Xue, Z., Kim, J., Mito, S., Kitamura, K., Matsuoka, T., 2009. Detecting and Monitoring CO2 With P-Wave Velocity and Resistivity From Both Laboratory and Field Scales. SPE International Conference on CO2 Capture, Storage, and Utilization, 2009, pp. 277–282. https://doi.org/10.2118/126885-MS.

Yang, L., Sun, Q., Hu, J., Li, C., 2021. Effects of temperature and pressure on electrical conductivity and wave velocity of basalt: a review. Acta Geodaetica Geophys. 56, 177–191. https://doi.org/10.1007/S40328-020-00323-3/FIGURES/9.

Zaima, K., Katayama, I., 2018. Evolution of elastic wave velocities and amplitudes during triaxial deformation of Aji granite under dry and water-saturated conditions. J. Geophys. Res. Solid Earth 123, 9601–9614. https://doi.org/10.1029/2018JB016377.

Zang, A., Oye, V., Jousset, P., Deichmann, N., Gritto, R., McGarr, A., Majer, E., Bruhn, D., 2014. Analysis of induced seismicity in geothermal reservoirs – an overview. Geothermics 52, 6–21. https://doi.org/10.1016/J.GEOTHERMICS.2014.06.005.

Zhang, Y., Park, H., Nishizawa, O., Kiyama, T., Xue, Z., 2017. Fluid distribution effects on P-wave velocity of CO2/brine saturated rocks: a comparison study and implications for CO2 Storage monitoring using seismic method. Energy Procedia 114, 3786–3792. https://doi.org/10.1016/J.EGYPRO.2017.03.1509.

Zhang, Y., Jackson, C., Krevor, S., 2022a. An estimate of the amount of geological CO2 storage over the period of 1996-2020. Environ. Sci. Technol. Lett. 9, 693–698. https://doi.org/10.1021/ACS.ESTLETT.2C00296/SUPPL_FILE/EZ2C00296_SI_002.XLSX.

Zhang, T., Zhang, W., Yang, R., Cao, D., Chen, L., Li, D., Meng, L., 2022b. CO2 injection deformation monitoring based on UAV and InSAR technology: a case study of Shizhuang Town, Shanxi Province, China. Remote Sens. 14, 237. https://doi.org/10.3390/RS14010237.

Zhang, B., Yang, F., Hu, D., Zhou, H., 2023. Laboratory study on injection-induced fault activation and slip behavior on fractures with specified roughness in sandstone. Rock Mech. Rock. Eng. 56, 7475–7494. https://doi.org/10.1007/S00603-023-03439-4/FIGURES/16.

Zhou, X., Liu, X., Wang, X., Zhang, S., Zhang, H., Gu, Z., Zhang, Y., Wei, X., 2025. Acoustic monitoring and structural damage evaluation of tensile fracture in various materials using optical fiber sensing. Phys. Fluids 37, 27184. https://doi.org/10.1063/5.0256902/3336660.

Zhubayev, A., Houben, M.E., Smeulders, D.M.J., Barnhoorn, A., 2016. Ultrasonic velocity and attenuation anisotropy of shales, Whitby, United Kingdom. Geophysics 81, D45–D56. https://doi.org/10.1190/GEO2015-0211.1/ASSET/IMAGES/LARGE/FIGURE10.JPEG.

Zoback, M.D., Gorelick, S.M., 2015. To prevent earthquake triggering, pressure changes due to CO2 injection need to be limited. Proc. Natl. Acad. Sci. 112, E4510. https://doi.org/10.1073/PNAS.1508533112.